Quenched primary melt in Ramlat as Sahmah 517 – snapshot of ureilite anatexis in the early solar system

[1] Åke V. Rosén

[1] Jonas Pape

[1,2] Beda A. Hofmann

[3] Edwin Gnos

[4] Marcel Guillong

[1]Institute of Geological Sciences

University of Bern

Baltzerstrasse 1+3, 3012 Bern, Switzerland

ake.rosen@geo.unibe.ch

[2]Natural History Museum Bern

Bernastrasse 15, 3005 Bern, Switzerland

[3]Natural History Museum of Geneva

1, Route de Malagnou, 1208 Geneva, Switzerland

[4]Institute of Geochemistry and Petrology

ETH Zurich

Clausiusstrasse 25, 8092 Zurich, Switzerland

Abstract

Ureilites are the second largest group of achondrite meteorites but consensus is still lacking on the nature of their precursors, melting processes and the genetic relationship between monomict ureilites and brecciated ones. The recently found ureilite Ramlat as Sahmah 517 is of special interest in this context. This meteorite lacks shock features in its primary silicates and belongs to a rare augite- and chromite-bearing subset of the monomict ferroan ureilites. It hosts abundant intergranular glass veinlets speckled with pyroxene and metal globules. Detailed petrographic investigations show that the Si-Al rich glass represents quenched anatectic melt that was present prior to formation of the reduced olivine rims by incomplete low-pressure equilibration (smelting) of carbon and silicates. The melt facilitated smelting which, along with rapid crystallization of secondary pyroxene, modified the originally trachyandesitic melt. Melt-silicate equilibrium preceding these events is constrained by modelling using MELTS and the first reported in-situ measurements of LREE-enriched glass that is largely complementary to the depleted mafic silicates in monomict ureilites. The inferred major element composition of the partial melt that formed in RaS 517 is similar to that of trachyandesite in Almahata Sitta but RaS 517 lacks phosphates which are abundant in the Almahata Sitta trachyandesite and in alkali-rich feldspathic clasts in polymict ureilites. The LREE-depletion in the dominant monomict ferroan ureilite population can be explained by the formation of melt fractions similar to the glass in RaS 517 after initial rapid melting of phosphates. These finds provide evidence for a genetic relationship between ferroan ureilites and lithologies similar to the Almahata Sitta trachyandesite and further suggest that these ureilites formed by partial melting of P- and alkali-rich precursors with trace element concentrations similar to equilibrated ordinary chondrites. Quenched Si-Al rich glass also occurs in magnesian ureilites but has lower concentrations of alkalis and LREE-depleted trace element signatures which can reflect more depleted compositions at the onset of partial melting. The evidence presented here favors a scenario in which the primary ureilite differentiation was driven by gradual heating from radioactive decay with resulting temperatures (>1100 °C) being maintained until disruption of the ureilite parent asteroid.

1. Introduction

With more than 500 individually classified meteorites, ureilites make up the second largest group of achondrites. Ureilites are ultramafic rocks largely consisting of Mg-rich olivine and pyroxene. Commonly occurring reduced metal speckled olivine rims and carbon-rich intergranular pockets contribute to a conspicuous ureilitic texture. On a large scale ureilites can be subdivided into unbrecciated or monomict samples and brecciated samples that are polymict or dimict. Monomict rocks display homogenous olivine and pyroxene core compositions which distinguish the less abundant type of ureilites with high mineral magnesium numbers (Mg#=Mg/(Mg+Fe)) from the much more common type of less magnesian ureilites (Downes et al., 2008). Pigeonite (molar wollastonite contents (Wo) of 520%) is the most common pyroxene variety in ureilites while augite-bearing ureilites make up a smaller subgroup. Augite in such samples is typically sub- to anhedral with crystals constituting a minor to large portion of the main mineral assemblage, and commonly exists alongside olivine enclosed in large low-Ca pyroxene grains (e.g., Goodrich et al, 2009). Similar assemblages have been described from polymict ureilites (Ikeda and Prinz, 2001; Kita et al., 2004) where these "Type II clasts" additionally were found to contain magmatic inclusions. Augite-bearing samples occur in both the more ferroan group of ureilites and in the magnesian population. Among magnesian augite-bearing ureilites, some have been found to contain melt inclusions in olivine and pyroxene (e.g., Goodrich 2009). Previous studies (e.g., Goodrich et al., 2001; Goodrich et al., 2009) have suggested that these inclusions represent primary liquid which was enclosed when the host minerals crystallized from magma. This interpretation is, however, contradicted by later studies which have argued that the porosity was likely insufficient to sustain large melt volumes during ureilite anatexis (e.g., Warren 2012). Oxygen isotopic ratios in ureilites are heterogeneous and do not conform to a mass-dependent fractionation trend (Clayton and Mayeda, 1996) which indicates an incomplete homogenization of the ureilite parent asteroid mantle. This can imply that the variability of olivine core compositions in different ureilite samples is an inherited feature, to some extent. Alternative explanations, such as early oxidation of heterogeneously distributed metal by initially accreted ice (Sanders et al., 2017) have, however, been suggested for both the heterogeneous oxygen isotopic ratios and the variability of silicate core compositions in ureilites. Recent Cr, Ti, Mo stable isotope and trace element studies have shown that the ureilite precursor material came from an isotope reservoir distinct from carbonaceous chondrites and more similar to ordinary chondrites (Qin et al., 2010; Yamakawa et al., 2010;

Warren, 2011; Barrat et al., 2016a; Budde et al., 2017). The origin of the relatively large amounts of carbon in ureilites still remains unresolved although a recent C isotope study (Barrat et al., 2017) is consistent with mixing of two sources of carbon showing a correlation of carbon isotopes with molar forsterite contents in olivine (Fo) such that Mg-rich ureilites show lighter C isotope compositions.

Ureilites are most commonly viewed as restitic lithologies formed from partial melting (e.g., Warren and Kallemeyn, 1992; Barrat et al, 2016b). The differentiation processes involved, and the detailed nature of ureilite precursors, remain largely unresolved but trace element studies have provided some constraints on the petrogenesis (e.g., Kita et al., 2004; Barrat et al., 2015; 2016b). These studies indicate that differentiation started with segregation of FeNi-S melts, after which fractional melting of the silicate residue led to the depletion of incompatible elements in ureilites. So far there have been no reported observations of melts enriched in incompatible elements which can directly connect common monomict ureilites to these processes. The timing of ureilite parent asteroid accretion and differentiation has been investigated using various radioisotope systems (Torigoye-Kita et al., 1995; Baker et al., 2012; Bischoff et al., 2014; Budde et al., 2015) and thermal modelling (Goodrich et al., 2015), which together point to an assembly more than ~1 Myr after the formation of calciumaluminum-rich inclusions (CAIs), followed by melt segregation and crystallization until 5-6 Myr after CAI formation. These dates represent a critical time interval in the history of the solar system. Heating by decay of primordial ^{26}Al is generally assumed to have driven the differentiation of early formed parent bodies including the ureilite parent asteroid (e.g., Goodrich et al., 2010). Several authors (e.g., Warren and Kallemeyn 1992; Goodrich et al., 2004; Warren and Huber 2006; Ikeda 2007) have suggested that the ureilite parent asteroid was still hot at the time of disruption. Recently, impact heating was proposed as an alternative mechanism to form albitic melt clasts found in ureilite breccias (van Kooten et al., 2017). Combined chronology of such clasts is otherwise inconsistent with the sub-canonical initial ^{26}Al/^{27}Al suggested by Schiller et al. (2015).

We present a study of the newly discovered augite-bearing monomict ureilite Ramlat as Sahmah 517 with special focus on the abundant intergranular glass. The combination of the rare petrographic observations and the pristine nature of this sample makes it uniquely suitable for in-depth investigations of primary ureilite silicate differentiation, intimately

connected with mantle formation in an early solar system asteroid and events leading up to the final disruption of the ureilite parent

body. These topics are addressed through detailed petrographic studies and in-situ trace element analyses.

2. Sample and analytical methods

2.1. Sample

Petrographic analyses were performed on a round one-inch thin section and a doubly polished slice prepared from the Ramlat as Sahmah 517 monomict ureilite, retrieved in 2015 through the Omani-Swiss Meteorite Search Project (Meteoritical Society Database, accessed December 28, 2017). The original material consisted of a single 16 g stone with minor signs of terrestrial weathering and abundant fusion crust.

2.2. EMPA and SEM

Mineral compositions and backscattered electron (BSE) images were obtained by electron microprobe analysis (EMPA) using a JEOL JXA-8200 Superprobe and scanning electron microscope (SEM) at the Institute of Geological Sciences, University of Bern. EMPA were performed with acceleration voltage and beam current set at 15 kV and 15-20 nA, respectively, during spot analyses of olivine and pyroxene with a focused beam and extended counting times of 120 s (peak) in order to improve measurement precision for minor oxides. EMP analyses in glass were performed with lower beam current (10-15 nA) and a defocused beam (1-7 μm) diameter (depending on the width of the analyzed glass surfaces), attempting to minimize alkali loss. Natural and synthetic silicate and oxide reference materials were used for calibration. Compositional maps were obtained, from selected areas, using step sizes between 0.5 and 1.5 μm and dwell times set between 90 and 120 ms. SiO_2 and Al_2O_3 concentrations in glass were calculated in selected compositional maps, using XMapTools (Lanari et al, 2014) where sufficient EMPA spots for standardization could be obtained. Several thin glass veinlets were only analyzed using SEM-EDX.

2.3. Trace elements

Lithophile trace element concentrations in olivine, pyroxene and glass were measured in-situ with laser ablation SF-ICP-MS at the Institute of Geochemistry and Petrology, ETH Zurich. Details of analytical instruments are described in Guillong et al. (2014). Ablation times were 30-40 s for individual measurements at energies of 3.5 J/cm^2 and repetition rates of 5Hz. Spot sizes were 13 μm for glass and between 19 and 51 μm for olivine, augite and low-Ca pyroxene. NIST610 was used as a primary reference material (RM) with identical ablation conditions as the sample and BCR-2G was used as secondary RM to test for accuracy. Al_2O_3 in glass and average SiO_2 in mafic silicate cores obtained by EMPA measurements (1-2 μm beam diameter on glass and focused beam on silicate cores) were used for internal

standardization. Measured CaO in olivine and pyroxene agree well with EMPA data. Results for 10 measurements on secondary RM BCR-2G gave precisions of 1-6% RSD and accuracy better than 10% for rare earth elements (REE).

3. Results

3.1. Petrography of RaS 517

The sample consists mainly of olivine, low-Ca pyroxene (here consistently used for primary pyroxene with Wo <5) and augite (Fig. 1a) in average proportions of 59:32:9, estimated from spatial distribution of mineral measured in BSE images, but showing large cm-scale variations. These minerals form an equilibrated texture with no apparent shock features. Augite occurs as subhedral grains and as inclusions, alongside rounded olivine, in low-Ca pyroxene. Olivine grains have characteristic reduced rims which were also observed where olivine occurs as inclusions in low-Ca pyroxene (Fig. 1b). Carbon phases occupy less than 2% of the studied sections and consist mostly of graphite, some as well-developed laths enclosed in low-Ca pyroxene (Fig. 1b), and minor diamond associated with "disordered" graphite (Raman spectra show diamond and ordered graphite bands in addition to D1 and D2 graphite bands, Supplement figure S1). Large (<1.7 mm) skeletal grains of chrome-spinel were observed in both sections. This spinel shows scalloped grain edges towards an intergrown carbon-metal assemblage and higher optical reflectivity where grain segments are not in contact with carbon phases (Fig. 1c).

Thin (<40 µm wide) fringes of glass extend as veinlets around all phases with an estimated total abundance of ≤1 vol%. Euhedral high-Ca pyroxene (here consistently used for secondary pyroxene with Wo >20) has crystallized on reduced olivine rims, in contact with glass, with fine intergrowths of reduced olivine and the secondary pyroxene (Fig. 2a-b). Secondary high-Ca pyroxene in glass veinlets is also found on primary low-Ca pyroxene rims. Glass surrounding primary augite and low-Ca pyroxene additionally, more rarely, hosts enstatite grown as fine dendrites on augite rims (Fig. 2c) Spinel-associated glass encloses µm-sized euhedral spinel grains and fine-grained mixtures of sub µm-sized spinel and pyroxene interstitial to surrounding silicates (Fig. 2d). Accessory phases include minor rounded blebs of metal and Cr-rich sulfides, mainly daubréelite intergrown with troilite, more rarely brezinaite. Metal-, sulfide globules and minor (Fe,Ni)-phosphide are hosted in glass veinlets. The globules commonly form linear trails extending into surrounding primary phases or are enclosed in secondary mineral grains (Fig. 2a-e).

3.2. Primary mineral compositions

Results from electron microprobe analyses (EMPA) are summarized in Table 1. The cores of olivine grains have homogenous compositions with average Fo 77. Augite and low-Ca pyroxene cores on average have Wo 34, 4 and Mg# 81, 80 respectively, with very little variation. Rims of olivine and pyroxene generally have lower FeO contents, most notably in olivine. Spinel compositions range from chrome numbers (Cr#=(Cr/(Cr+Al)) of 64 to 68 and Mg# 46 to 94 with lower values representing less reduced grain segments with higher reflectivity (Fig. 1c).

3.3. Composition of glass and of phases crystallized in contact with glass

Measured oxide concentrations in glass and associated phases are summarized in Table 2. Glass compositions are dominated by SiO_2, Al_2O_3 and Na_2O, with SiO_2 concentrations ranging from 61 to 83 wt% according to the combined suites of EDX and microprobe analyses obtained from two sample sections. The lowest SiO_2 concentrations were mainly observed in thin veinlets which were analyzed by SEM-EDX. The large range of SiO_2 concentrations is, however, clearly visible in element maps (Fig. 3) and in perfect agreement with quantified SiO_2 and Al_2O_3 concentrations in EMPA standardized maps (Fig. S2). In spite of using a defocused beam, the generally low EMPA totals indicate substantial Na loss during analysis. EDX data thus reflect the range of alkali concentration in the glass more accurately and allowed for the full range of corresponding SiO_2 and Al_2O_3 to be measured in the glass veinlets. Secondary pyroxene and spinel associated with glass have higher Mg# than the primary assemblage. Euhedral high-Ca pyroxene grains have Wo corresponding to augite but closely approaching diopside.

3.4. Trace elements

Results from trace element laser ablation ICP-MS measurements are listed in Table 3. Glass compositions were measured in twelve spots with four measurements showing slightly elevated CaO or FeO compared to EMPA values. These deviations can be explained by minor ablation of secondary phases hosted in the glass and show no resolvable influence on measured concentrations of most trace elements. Lithophile trace elements measured in glass show strong enrichment in incompatible elements (Rb, LREE) and positive anomalies of Ba, Zr, Sr, and Eu. Incompatible trace element concentrations in mafic silicates decrease in the order of augite > low-Ca pyroxene > olivine.

4. Discussion

4.1. Interstitial glass in RaS 517 and other ureilites

Al-Si-rich glass along grain boundaries of major silicates has been described from a handful of monomict ureilite samples with Fo 74-80 and additionally in a few samples with Fo 82-87, where the glass is generally enclosed in mafic silicates (Table 4; references therein). Together these samples largely cover the major mineral compositions in the ureilite population. This shows that Si-Al-rich melts formed in the source regions of both the dominant ureilite type (lower Mg#) and the significantly less abundant type of more magnesian ureilites (higher Mg#). A large proportion of monomict glass-bearing ureilites are of the less common augitebearing variety, but all pyroxene type lithologies are represented (Table 4).

RaS 517 shares many conspicuous textural features with other ureilites in which glass has previously been observed, especially those with lower Mg# for mineral cores. Most strikingly, LEW 88774 exhibits many similarities with the RaS 517 mineral assemblage and mineral compositions. These similarities include compositionally zoned grains of chromespinel with thin rims of glass and late redox associated accessory components, previously described in detail by Goodrich et al. (2014). The same study showed that chrome-spinel more commonly occurs in glass-bearing ureilites. Additionally, glass surrounding primary augite in LEW 88774 hosts magnesian pyroxene that apparently nucleated as µm-sized, dendritic aggregates around partly consumed augite grains. Similar textures have been described from the majority of ferroan samples listed in Table 4 (references therein). High-Ca pyroxene crystals hosted in glass are known from most glass-bearing ureilites, where the morphology and compositional variability of the crystals indicate rapid crystallization. This suggests that ureilites of a wide variation in composition and mineralogy experienced late quenching under similar conditions. Various authors (e.g., Rubin 2006; Warren and Rubin 2010; Janots et al, 2011; Godrich et al., 2014) have offered different explanations for the genesis of the Si-Al-rich glasses, often invoking a shock-related origin. Several glass-bearing ureilites record different shock histories than RaS 517 which, as opposed to e.g., NWA 766 and LAP 03587, does not show fine recrystallization/mosaicization of pyroxene or olivine and also no other typical signs of lower shock degrees in these minerals.

4.2. Late stage modification of melt composition

Melt experiments (Feldstein et al., 2001; Usui et al., 2015; Lunning et al., 2017) clearly show that, although silicic melts can be produced by partial melting of ordinary chondrite- or

Rumuruti chondrite-like material, the wide range of SiO_2 concentrations preserved in RaS 517 glass and similar material in other ureilites is not compatible with the silicate mineral compositions found in ureilites. Instead, partial melting of RaS 517 and ureilite precursor material in general would produce andesitic or basaltic melts. The large range in SiO_2 found in ureilite glass can be the result of late rapid crystallization of mainly high-Ca pyroxene, along with redox reactions that involved primary silicates reacting with adjacent carbon phases, leading to the addition of SiO_2 to the melt. Elemental EMPA maps (Fig. 3) show bands with high Mg content along primary olivine and pyroxene grain boundaries which correspond to secondary enstatite dendrites. Adjacent to carbon pockets, these elevated Mg contents commonly coincide with Si-enriched spots in glass veinlets that clearly stand out from the otherwise smooth gradations of Si contents in the glass. Glass veinlets typically extend along thin weak zones within primary pyroxene grains which show elevation of Mg where the host phase has reacted with the melt (Fig. 3a). The Al contents of the glass show a negative correlation with Si contents. In several veinlets, Si-rich glass in direct contact with carbon phases exhibits a gradual decrease of Si with increasing Al contents and distance from the carbon source. This is interpreted as mixing of the melt with SiO_2 that was derived from the reduction of mafic silicate minerals. Glass with high Al-contents hosts high-Ca pyroxene, which overall is the dominant associated secondary phase (Fig. 3b).

Direct smelting of olivine can be summarized by reactions (1) and (2), suggested by Warren and Rubin (2010) in a similar context:

$$2C + 2(Mg_3FeSi_2O_8) \rightarrow 3(Mg_2SiO_4) + 2Fe + 2CO + SiO_2 \quad (1)$$

or

$$3C + 3(Mg_3FeSi_2O_8) \rightarrow 4(Mg_2SiO_4) + 3Fe + 3CO + MgSiO_3 + SiO_2 \quad (2)$$

These predict production of one mole of SiO_2 by reduction of four moles of olivine (Fo 75) (Reaction 1) or, in the case of simultaneous production of enstatite (Reaction 2) one mole of SiO_2 per mole of fayalite in olivine reduced. Predicted reaction products include a volume of SiO_2 equivalent to ~9-13% of the primary olivine volume subjected to complete reduction which, judging by the small volume of glass present, could account for the most felsic glass compositions. Reaction (2) or similar reactions, with primary pyroxene as reactant, could correspond to enstatite dendrites and localized associated strong Si-enrichment observed in RaS 517. Judging from the spatial distribution of strong Si-enrichment these are, however,

not efficient enough to account for the observed amount of olivine rims with reduced composition.

Studies on metallurgically relevant reactions (e.g., Sarma et al., 1996) describe the overall reduction of FeO-poor slag by initially solid carbon through a reaction series starting with:

$$FeO_{(liq)} + (1 + x)C_{(s)} \rightarrow [Fe - C_x] + CO_{(g)} \quad (3)$$

In this reaction production is limited by diffusion of bulk FeO through liquid slag to the reaction interface. In addition, pressure conditions should not inhibit gas production. Applied to ureilites, this requires diffusive transport of FeO to carbon phases or C dissolved in metal, since the solubility of C in silicate melts, even at favorable conditions, is several orders of magnitude lower than in metal (Dasgupta et al., 2013). This likely limits initial reduction of FeO and production of CO to sites with carbon or metal alloys adjacent to silicate melts containing FeO. As such, reduction by solid carbon cannot fully explain the prominent reduced olivine rims in general and especially not the observation that olivine enclosed in low-Ca pyroxene shows similar reduced rims (Fig. 1b). In accordance with Sarma et al. (1996), $CO_{(g)}$ produced by reaction (3) would diffuse away from the reaction interface along the melt and further reduce $FeO_{(liq)}$ by:

$$FeO_{(liq)} + CO_{(g)} \rightarrow Fe_{(s)} + CO_{2(g)} \quad (4)$$

followed by

$$CO_{2(g)} + C_{(s)} \rightarrow 2CO_{(g)} \quad (5)$$

The full series of reactions (3-5), where $CO_{(g)}$ and $CO_{2(g)}$ together act as an electron conveyor, can effectively remove FeO from the melt while increasing the internal pressure by rapidly producing more gas. In turn, pre-existing melt would be forced into less competent structures, such as present or relict grain boundaries, assuming a sufficient confining pressure. FeO-depleted melt could then start re-equilibrating with silicate rims and, since Fe-Mg interdiffusion is related such that $D_{Fe\text{-}Mg,Fa} > D_{Fe\text{-}Mg,Fo} > D_{Fe\text{-}Mg,Cpx}$ (Chakraborty, 1997; Müller et al., 2013), apparent reduction would mostly affect olivine rims and primary silicates directly adjacent to the propagating melt veinlets.

Compositional trends in RaS 517 glass indicate a homogenous melt composition preceding rapid cooling and pyroxene crystallization. Evidently, silica concentration increased

inhomogenously at a late stage. The $CaO:Al_2O_3:SiO_2$ system ternary diagram (Fig. 4.) shows two diverging compositional trends. Gradual decrease of CaO with increasing SiO_2/Al_2O_3 corresponds to removal of a melt component similar to secondary high-Ca pyroxene. Based on the average composition of the secondary high-Ca pyroxene (Table 2) this process was coupled with addition of SiO_2 to the melt. The most silicic glass has incorporated additional SiO_2 after most CaO had crystallized as pyroxene. Similar patterns are evident for TiO_2 and to a lesser extent for MgO. FeO was largely disconnected from this process in accordance with the preceding discussion on reduction of $FeO_{(liq)}$ and incomplete melt-silicate reequilibration. Na_2O/Al_2O_3 remained almost constant with increasing SiO_2, over the large range of concentrations measured with SEM-EDX, apart from a cluster of glass spots with slightly lower values. This glass is associated with metal, lacks secondary high-Ca pyroxene and could, since a similar pattern is seen for K_2O, indicate minor local crystallization of an unidentified alkali-rich phase. Compositional trends in the RaS 517 glass show that crystallization of secondary minerals and late redox reactions substantially reduced concentrations of FeO, MgO and CaO in the melt but had less apparent influence on Na_2O/Al_2O_3 which was similar to that measured in the present glass. CaO/Al_2O_3 in the unmodified melt is best represented by a mixture of secondary high-Ca pyroxene and glass with high Al_2O_3 and alkali contents, corresponding to the lowest measured SiO_2 concentrations. The highest concentrations of Al_2O_3 and alkalis were measured in a thin glass veinlet in between euhedral high-Ca pyroxene, which apart from metal/sulfide globules, is the only secondary phase that was identified in this veinlet (Fig. 2b). Patches that appear darker than the surrounding glass in reflected light were observed in this veinlet but were too small to analyze. These could potentially correspond to either cristobalite, which was described in a study on Asuka 881931 (Ikeda 1999), or minor silica patches similar to those seen in LEW 88774 (Goodrich et al. 2014). Minor crystallization of a pure silica phase in the melt that was least affected by crystallization of pyroxene could thus have widened the observed range of correlated element concentrations in the glass slightly.

Combined petrographic observations on glass and associated phases in RaS 517 reveal late rapid processes which were associated with a decrease of temperature and pressure. Reduced olivine rims are found in most ureilites and, like several previous authors, (e.g., Warren and Huber 2006; Ikeda 2007; Downes et al. 2008) it is compelling to connect the genesis of these to the disruption of the ureilite parent asteroid. The proposed mechanism for the formation of

Mg-rich olivine rims in RaS 517 relies on prerequisites similar to those outlined by Warren and Huber (2006). An impact, which substantially reduced the mass of the ureilite parent asteroid in an anatectic state, would trigger initial production of $CO_{(g)}$ through pressure loss, also in segments which were not affected by major shock. Once started, reaction 3-5 would progress, unless a sufficient drop in temperature caused them to halt before complete consumption of reactants. This could subsequently be caused by overstepped confining pressure due to gas production, leading to final disruption and quenching. At the final quenching stage, secondary high-Ca pyroxene crystallized on already reduced olivine rims. This event is constrained by textural relations including secondary high-Ca pyroxene which partly encloses reduced olivine rims (Fig. 2a) and generally by secondary mineral overgrowth of metal globules in primary mineral-glass interfaces (Fig. 2a-d). Mass balance of major and minor elements in glass and associated phases in RaS 517 dictates that the melt could not have formed solely by direct shock-melting of the observed primary mineral assemblage. Such shock-melts would have a composition corresponding to a mixture of pyroxene and olivine. Also, shock effects in associated pyroxene and olivine are lacking. Beside the forsterite-rich olivine rims commonly found in ureilites, observations of pyroxene rims with reduced composition in association with glass (Fig. 2 and Fig. 3) suggest that late redox reactions were mediated by contact with melt. Similar observations have been reported in studies on glasses in ferroan monomict ureilites (Ikeda, 1999; Warren and Rubin, 2010) and from this it can be inferred that glass in RaS 517 likely represents anatectic melt that was present at the time of the ureilite parent asteroid disruption.

4.3. Primary melt composition

Reconstruction of the melt composition prior to formation of olivine reduction rims is difficult since the net melt volume and composition changed. This was caused by dilution of the primary melt with silica and reduction of $FeO_{(liq)}$ followed by incomplete Fe-Mg meltsilicate re-equilibration and crystallization of dominantly high-Ca pyroxene. Further melt loss might have followed due to gas-driven melt expulsion connected to the late pressure loss event. Additionally, modal estimates in thin sections are biased by preferential loss of glass from polishing and anisometric distribution of glass veinlets. Homogenous primary silicate and spinel core compositions allow for equilibration conditions of the RaS 517 mineral assemblage and a corresponding partial melt composition to be explored using conventional geothermometry and thermodynamic modelling. Lunning et al. (2017) found that melts

produced experimentally by partial melting of a Rumuruti chondrite starting material show reasonable agreement with theoretically derived compositions (i.e., trachyandesites) at 1140 °C using MELTS (Ghiorso and Sack, 1995; Asimow and Ghiorso, 1998).

MELTS calculations, geothermometry and oxybarometry were used to model the partial melt composition corresponding to the equilibrated primary mineral assemblage in RaS 517. Averaged pyroxene and olivine core compositions (Table 1) were used for the two-pyroxene geothermometer of Brey and Köhler (1990) and the MELTS geothermometer-oxybarometer calculator. Spinel with highest FeO contents was assumed to be representative for the oxygen fugacity at equilibrium. The composition of this spinel is similar to that of spinel cores in LEW 88774 (Goodrich et al., 2014) and spinel formed by partial melting of an equilibrated L chondrite at 1200 °C and log fO_2 IW-1 (Feldstein et al., 2001). Bulk RaS 517 silicate composition, calculated from estimated modal abundances and average core compositions of olivine and pyroxene, was used in the MELTS calculations. Since a considerable fraction of the sample alkalis is hosted in the glass, a small weight fraction (0.5%) of glass with the lowest silica concentrations (see section 4.2) was added to this composition in the calculations. From calculated MELTS densities (g/cm^3), ~2.5 for liquid and ~3.3 for bulk, this fraction translates to a conservative <1.5 vol% melt at equilibrium, also considering quench crystallization of pyroxene. A modelled pressure of 100 bar, corresponding to the center of a body with a ~60 km radius was selected based on previously predicted pressures needed to stabilize graphite (Warren, 2012). Results are listed in Table 5 along with relevant input parameters. Calculated mineral compositions at 1140-1170 °C, in accordance with thermometry and oxygen barometry, are very similar to those measured in RaS 517. Above 1170 °C pigeonite (Wo 14) is predicted to completely replace augite. Calculated melt compositions are trachyandesitic but extend to trachytic at T<1150 °C (Fig. 5a). This may be due to a slight overestimation of the liquid silica component in the MELTS algorithm. The partial melt compositions obtained with MELTS were used to calculate the corresponding theoretical silica- and alkali-dependent, Fe and Mg exchange coefficients of olivine and liquid using equations by Toplis et al. (2005). The calculated exchange coefficients deviate less than 3% from those obtained with MELTS and thus suggest that the obtained liquid silica- and alkali concentrations are compatible with the main mineral assemblage although liquid compositions with 3 mol% less SiO_2 correlate slightly better with predictions based on the equations by Toplis et al. (2005) (Table 5).

352 The melt compositions calculated for partial melting of RaS 517 silicates are similar to
353 experimental melts obtained from an alkali-rich ordinary chondrite-like starting composition
354 (Usui et al., 2015) and the reported bulk composition of the Almahata Sitta trachyandesite
355 (Bischoff et al., 2014). This suggests that major- and minor element concentrations were
356 similar to ordinary chondrites in the precursor material of both RaS 517 and the Almahatta
357 Sitta trachyandesite even though the oxygen isotopic ratios (Clayton and Mayeda, 1996) and
358 comparatively large amounts of carbon in ureilites rule out actual ordinary chondrites as the
359 precursor of ureilites. Both the experimental melt and the Almahata Sitta trachyandesite have
360 slightly higher concentrations of SiO_2 than a mixture of glass with low SiO_2 and secondary
361 high-Ca pyroxene in RaS 517 with corresponding concentrations of alkalis (Fig. 5a), CaO
362 and Al_2O_3 (Fig. 5b). These differences are minor and could be due to small variations in
363 temperature and pressure or effective bulk composition in addition to unaccounted
364 crystallization products. The composition of Si-Al-rich glass in other ferroan ureilites,
365 exemplified by glass in LEW 88774, often represents close to perfect ternary mixtures of
366 CaO, Al_2O_3 and SiO_2 in glass with low SiO_2 and secondary pyroxene in RaS 517 (Fig. 5b).
367 Compared to the average bulk composition of ordinary chondrites, the concentration of Al_2O_3
368 in residual olivine and pyroxene in RaS 517 is lower. The CaO:Al_2O_3:SiO_2 ternary system
369 suggests that if average CaO/Al_2O_3 in ordinary chondrites is fully representative of RaS 517
370 prior to partial melting the accumulated partial melt had a slightly lower concentration of
371 CaO than the modelled MELTS liquids. Alternatively, bulk CaO/Al_2O_3 in RaS 517 was
372 slightly overestimated. Results from MELTS calculations and the preceding discussion show
373 that the glass observed in RaS 517 originated as trachyandesitic melt that formed through
374 partial melting of a bulk rock composition similar to the host material. The inferred
375 unmodified major element composition of this melt strongly resembles melts produced
376 experimentally by partial melting of alkali-rich chondrites and that of the Almahata Sitta
377 trachyandesite (Bischoff et al., 2014). Slightly higher final temperatures would lead to the
378 replacement of augite with pigeonite in the residual assemblage which in turn is consistent
379 with the overall more common occurrence of pigeonite-bearing ferroan ureilites.

380 **4.4. Trace elements**

381 REE concentrations in RaS 517 glass compared to those predicted by inverted partitioning
382 between primary pyroxene and melt provide additional strong evidence for melt-silicate
383 equilibrium. Melts reconstructed using known partition coefficients (Barrat et al., 2016b;

Severs et al. 2009) for clinopyroxene and orthopyroxene in dacitic melt have almost identical REE and Sr patterns as those in analyzed glass (Fig. 6a). Less pronounced Eu anomalies measured in glass show that an assumed similar partitioning behavior of Eu and Sr (Barrat et al., 2016b) is not valid for the stage of differentiation sampled by RaS 517. In single glass measurements the effect of rapid high-Ca pyroxene crystallization is mainly manifested as variable HREE concentrations. This variability could have been enhanced by a cooling rate dependent increase in partition coefficients between clinopyroxene and melt which is less pronounced for LREE (Mollo et al., 2013).

Barrat et al. (2016b) measured bulk lithophile trace elements in a series of leached ureilite samples and subdivided these into two different groups (A and B) based on LREE depletion and Eu vs Eu*. It is difficult to evaluate the significance of these variations. Pyroxene compositions and relative proportions of pyroxene and olivine vary strongly between and locally within ureilite samples. Low-Ca pyroxene in RaS 517 is clearly more depleted in LREE than augite and exhibits larger Eu anomalies, forming patterns that correspond to group B ureilites (Fig. 6b). The calculated average bulk REE pattern of primary olivine and pyroxene in RaS 517 combined is controlled by primary augite and corresponds to least depleted group A ureilites (Fig. 6b). REE patterns in RaS 517 minerals are similar to those reported from previous in situ studies of ureilites (Guan and Crozaz, 2000; Guan and Crozaz, 2001; Goodrich et al., 2009) which generally show decreasing REE and increasing depletion of LREE with lower Wo contents. This suggests that the REE concentrations and variable depletion of LREE observed in bulk ureilites are controlled by the proportions of sampled pyroxene and by their Wo contents at the time of partial melting.

The depletion of LREE in ureilites has been attributed to fractional melting of a precursor material with ordinary chondrite-like mineralogy and trace element composition which can produce bulk REE patterns that are consistent with in-situ measurements of silicates in RaS 517 and other ureilites (Barrat et al. (2016b). Assuming that partial melting followed after prograde metamorphism of such a precursor the melting mineral assemblage would likely resemble that of equilibrated ordinary chondrites. Albitic feldspar and phosphates are the major REE carriers in ordinary chondrites (Ward et al., 2017) and, within the mineral assemblage, are some of the first phases to melt upon heating (Feldstein et al., 2001). In equilibrated ordinary chondrites albitic feldspar and phosphates are present in amounts far exceeding those normally seen in ureilites. Apart from merrillite (“whitlockite”) seen in

albite-bearing porphyritic clasts in DaG 319 (Kita et al., 2004) and similar clasts in other polymict ureilites (Goodrich et al., 2017) one notable exception is the trachyandesite from Almahata Sitta, reported to carry abundant apatite (Bischoff et al., 2014). The trace elements pattern of this rock shows slight depletion of LREE relative to HREE and minor positive anomalies of Ba, Zr, Eu and Sr (Fig. 6c) which is inconsistent with early formed fractions of partial melt that have equilibrated with an undepleted source containing feldspar and pyroxene. Disequilibrium partial melting experiments on an L chondrite (Feldstein et al., 2001) show that the earliest silicate melts form rapidly and have trace element abundances largely controlled by the local availability of feldspar and phosphates. These melts are often slightly depleted in LREE and can have either positive or negative Eu anomalies. Rapid extraction of unequilibrated melt to form the Almahata Sitta trachyandesite has accordingly been suggested (Bischoff et al., 2014). An early stage removal of melt with similar composition as the Almahata Sitta trachyandesite could partially account for negative anomalies of Ba, Zr, Eu and Sr in the RaS 517 residue (Fig. 6c) and other ureilites (Barrat et al. 2016b). The negative Ti anomalies in the RaS 517 residue and in other ureilites suggest that Ti-rich phases such as ilmenite, which is commonly found in porphyritic alkali-rich clasts from DaG 319 (Kita et al. 2004), were consumed during early stages of melting. Disequilibrium melting of feldspar and phosphate, however, cannot account for the depletion of LREE relative to HREE in ureilites. A rapid early stage extrusion of melts with trace element concentrations similar to the trachyandesite in Almahata Sitta, from a source with ordinary chondrite-like composition, would leave residues with slightly higher LREE/HREE than the precursor material.

Average trace element patterns of glass in RaS 517 appear complementary with combined concentrations in olivine and pyroxene (Fig. 6c). However, the negative slope towards LREE and LILE in the residue along with the difference in magnitude of negative anomalies in the residue and positive anomalies in the glass, likely require more than one single stage of melting (i.e., fractional or dynamic melting) to form. If the residue was undepleted in LREE when melt production decreased, the enrichment of incompatible elements and positive anomalies of Eu, Ba and Sr seen in the RaS 517 glass (Fig. 6c) are expected from the last melt volumes that sampled feldspar. There are no phosphates in RaS 517 and apart from minor phosphide (Fig. 2e) no other P-rich phases. These observations suggest that most

447 phosphate had already been removed when feldspar was exhausted and melt production
448 ceased.

449 Crystallization of trachyandesitic melt modelled with MELTS (Table 5) at 1100-500 °C
450 would yield mafic silicates with Mg# ~55-75 and feldspar with An of ~40-1. These mineral
451 compositions correspond to those in some feldspathic clasts in DaG 319 which have
452 previously been measured for trace elements (Kita et al., 2004). The most alkali-rich
453 lithologies among clasts in DaG 319 contain feldspar (An 1-7) which have Ba/Sr values
454 similar to albitic (An ~10) feldspar in equilibrated ordinary chondrites (Kovach and Jones,
455 2010) and glass in RaS 517 (Fig. 6d). Assuming that the alkali-rich clasts in DaG 319 and
456 glass in RaS 517 have related precursors and that the clasts in DaG 319 represent early stage
457 melt fractions, very limited fractionation of Ba and Sr occured during melting and
458 crystallization. Surficial terrestrial contamination by Ba and Sr has previously been observed
459 in hot desert meteorites where it is typically associated with secondary barite/celestine and
460 easily recognizable in BSE images. Ba/Sr contamination mostly affects strongly weathered
461 samples (Zurfluh et al., 2016) and has clearly not influenced the constant pattern of in-situ
462 Ba/Sr in the RaS 517 glass.

463 Partition coefficients (D_i) of Ba and Sr for albitic feldspar obtained with the model of Blundy
464 and Wood (1991) were used to predict the concentrations of Ba and Sr in melts produced by
465 fractional melting of an ordinary chondrite-like mineral assemblage containing albitic
466 feldspar. Since both the EDX analyses of glass in RaS 517 (Table 2) and the calculated
467 partial melt compositions (Table 5) give Na/Al molar ratios close to one, a significant change
468 of partition coefficients due to increasing An in the melting assemblage was not considered.
469 Calculation parameters for fractional melting were identical to those previously used by
470 Barrat et al. (2016b) for initial melting of pyroxene, olivine and feldspar with additional
471 values of D_{Ba} for clinopyroxene and orthopyroxene adopted from Severs et al.
472 (2009).

473 Representative results for early and late formed melts, respectively, are included in Fig. 6d.
474 The calculations predict small changes in concentrations of Ba and Sr moving from early
475 melt fractions to the last fractions of melt forming before feldspar is completely exhausted in
476 the melting assemblage. Early formed melt fractions are predicted to have slightly higher
477 Ba/Sr and lower concentrations of Ba than the last fractions (Fig. 6d). Partition coefficients of
478 Ba and Sr vary with temperature in addition to An in the melting feldspar but this example

show that the alkali-rich clasts in DaG 319 could have formed as early melts in similar precursors as that of the glass in RaS 517. Slightly lower Ba/Sr values in some of the feldspar grains in DaG 319 correlate with their anorthite contents (An 14-39) which suggest that these grains formed by fractional crystallization from alkali-rich melts with similar Ba/Sr as the glass in RaS 517. Additional clasts clearly formed from less alkalic melts and show either moderate (feldspar with An 35-57) or strong (feldspar with An 84-94) depletion of Ba relative to Sr (Fig. 6d).

The dissimilarity of the feldspathic clasts in DaG 319 was recognized by Kita et al. (2004) who suggested that the low abundances of Ba, Ti and K in the clasts with high anorthite contents may require a source depleted in these elements. Feldspar in moderately depleted clasts (An 35-57) could potentially be products of fractional crystallization from partial melts, less alkalic than RaS 517 glass, which formed in ferroan ureilites that experienced higher equilibration temperatures. The trace element concentrations in strongly depleted clasts (feldspar with An >80) in DaG 319 would instead attest to several additional steps of melting and crystallization if these lithologies were to have originated from an undepleted precursor similar to that of RaS 517.

Combined observations of trace element concentrations suggest that the restite signature in RaS 517 formed after removal of partial melts similar in composition to the Almahata Sitta trachyandesite and albitic rocks in polymict ureilites which, in addition to phosphates commonly contain ilmenite (Ikeda and Prinz, 2001; Kita et al., 2004; Bischoff et al., 2014; Goodrich et al., 2017). Unlike the dominant pigeonite-bearing ureilite variety, RaS 517 and other augite-bearing ferroan ureilites equilibrated at slightly lower temperatures, are less depleted in incompatible elements and were therefore more likely to preserve recognizable partial melt fractions after phosphates and feldspar had been exhausted and melt production halted. The trace element characteristics of this ureilite are unique as they provide records from the formation of the largest monomict ureilite group and early formed melts represented by Almahata Sitta trachyandesite and the dominant type of feldspathic melt clasts found in polymict ureilites as well as evidence for a genetic relation between these populations.

4.5. Bimodal ureilite precursor

The commonly cited range of ureilite olivine core compositions (e.g., Goodrich et al., 2004; Barrat et al., 2016b; Sanders et al., 2017) does not appear to be caused by a gradual process connected to differentiation. Ureilite olivine cores compose two distin populations (Downes

et al., 2008). The larger ferroan population generally has Fo 76-80 similar to equilibrated L and H chondrites while the smaller sampled population of magnesian ureilite olivine most commonly has Fo 82-88 but ranging above 90. Both populations to some extent host Al-Sirich melts preserved as glass. Feldspar with An >80 in DaG 319 (Fig. 6d) cannot have formed as products from melting of an alkali-rich precursor without involving extreme fractionation processes and is instead likely derived from a depleted parent source that could be related to the source of melt inclusions in the magnesian ureilites FRO 90054/93008 and Hughes 009. These melt inclusions are depleted in LREE relative to HREE and largely consist of anorthite normative glass (Goodrich et al., 2009). Ferroan ureilites are associated with alkali-rich melts and are, as this study suggests, further distinguished by their trace element characteristics. The largely albite normative melt composition sampled in RaS 517 is expected after prograde metamorphism followed by melting of a precursor with major- and trace element concentrations similar to ordinary chondrites. Feldspar in chondrules from equilibrated ordinary chondrites is albite dominated (Kovach and Jones, 2010) while compositions similar to magnesian ureilite glasses, in ordinary chondrites, are preserved in mesostasis of type I chondrules of petrographic type 3 (Alexander and Grossmann, 2005; Jacquet et al., 2015) and rarely as anorthitic feldspar in L-LL chondrules of petrographic type 4. Preservation of similar chemical signatures in ureilites clearly implies that the ureilite dichotomy is primordial and that mixing of the two current populations was very limited during silicate differentiation on the ureilite parent asteroid.

4.6. Carbon in ureilites

The recent discovery of unusually large diamonds in a sample from the Almahata Sitta strewnfield (Miyahara et al., 2015) together with earlier spectroscopic studies on ureilite diamonds and their noble gas signatures (e.g., Miyamoto et al., 1993) clearly show that the widespread occurrence of diamond in ureilites did not result solely from shock. The large diamonds occurring in Almahata Sitta were subsequently inferred to have experienced slow growth, at pressures exceeding 2 GPa, which, if formed in-situ, would imply an ureilite parent asteroid diameter of ~1000 km or more (Miyahara et al., 2015). On Earth, most known natural diamond-forming reactions involve fluid-assisted reduction or oxidation of carbon species, leading to isotope fractionation (Dobrzhinetskaya, 2012; Stachel and Luth, 2015). Analogous extra-terrestrial material, which displays mica, graphite and associated phases similar to eclogites on Earth, does not contain diamond, despite an estimated parent body

543 diameter exceeding 1000 km (Kimura et al., 2013). Direct formation of diamond from
544 graphite on the ureilite asteroid would most likely require pressures exceeding 10 GPa and
545 temperatures above the corresponding ureilite liquidus (Sumiya et al., 2004). In RaS 517,
546 graphite laths, which are enclosed in large low-Ca pyroxene grains, indicate that graphite was
547 the stable carbon polymorph during ureilite mantle formation. This is consistent with the
548 observed association of ureilite diamond with disordered graphite (Fig. S1) which could
549 indicate thermal graphitization of diamond (e.g., Willems et al., 2004). The combined
550 observations of well crystallized graphite enclosed in pyroxene and partly graphitized
551 diamond suggest that the remnant diamond in this ureilite predates the primary stage of
552 silicate differentiation on the ureilite asteroid. A high-pressure fluid- or shock-related origin
553 of diamond in this sample can furthermore likely be excluded based on petrographic
554 observations and measured trace elements.

555 **4.7. Temperature state during asteroid disruption**

556 The observed late stage crystallization of various minerals from residual anatectic melt
557 provides some constraints on the final disruption of the ureilite parent asteroid given that this
558 evidently coincided with formation of commonly observed reduced olivine rims. Before
559 asteroid disruption, some amount of melt similar to that in RaS 517 was clearly still present
560 in several ferroan ureilites. In some magnesian ureilites, more calcic and depleted melt was
561 trapped in refractory mineral hosts. Irrespective of shock effects, these samples record quench
562 crystallization of pyroxene which was preceded by temperature conditions suitable to sustain
563 Al-Si-rich melts. Additionally, some amount of liquid was likely a prerequisite to allow
564 reduction of FeO and diffusion of reductants to form prominent reduced olivine rims. More
565 widespread occurrence of minute amounts of Al-Si-rich glass than has yet been recognized,
566 could potentially help explain the so far unidentified origin of homogenous LREE
567 enrichments located in the C-rich matrix areas of some monomict ureilites including Kenna
568 (Guan and Crozaz, 2000). Petrographic evidence in RaS 517 and conclusions of previous
569 ureilite studies (e.g., Warren and Huber 2006; Ikeda 2007; Downes et al., 2008) suggest that
570 the ureilite parent asteroid was partially molten at the time of disruption. Combined, these
571 observations are consistent with gradual heating by decaying ^{26}Al, possibly followed by slow
572 cooling, an effect that may have been enhanced as the heat source was partially removed by
573 fractional melting and melt extraction. Primary silicate differentiation of ferroan ureilite
574 precursors produced melts similar to those sampled in RaS 517 after exhaustion of

phosphates. It is therefore unlikely that albitic melt clasts in polymict ureilites generally formed due to impact heating after the primary differentiation had ceased.

5. Conclusions

Al-Si-rich glass in ureilite RaS 517 originated as trachyandesitic anatectic melt that formed intergranular veinlets in the region of the ureilite parent asteroid sampled by this meteorite. Abrupt pressure loss at a temperature exceeding 1100 °C led to apparent reduction of olivine rims, absorption of liberated silica in melt and rapid crystallization of pyroxene as final quench phases. This is consistent with textural observations, major chemistry, modelled melt compositions and in-situ trace element measurements. REE concentrations in mafic silicates and glass, along with feldspar normative components in glass, record fractional melting which ceased after feldspar was exhausted. Previous observations (Table 4) of texturally similar samples in the large population of monomict ferroan ureilite suggest a rather widespread occurrence of similar melts on the ureilite parent asteroid. The RaS 517 melt composition, which most likely is genetically related to melts produced from other ferroan ureilites and those preserved in the Almahata Sitta trachyandesite in addition to alkali-rich polymict ureilite clasts, favors a largely undisturbed primordial bimodality of ureilite precursors similar to undifferentiated ordinary chondrites. Preservation of primary trachyandesitic melt in direct association with reduction and quench textures connected to the ureilite parent asteroid disruption suggests sustained heating by radioactive decay up until a snapshot of the final state was recorded in RaS 517.

Acknowledgements

Addi Bischoff, Hillary Downes and one anonymous reviewer are gratefully acknowledged for helpful and constructive reviews; Chris Herd for the editorial handling. The authors additionally wish to thank Klaus Mezger for valuable discussions which contributed greatly to the manuscript. This work was supported by the SNF grant nr. CR33I2_152941. JP acknowledges additional support from the NCCR PlanetS.

References

Alexander C. M. O'D and Grossman J. N. (2005) Alkali elemental and potassium isotopic compositions of Semarkona chondrules. *Meteorit. Planet. Sci.***40**, 541-556.

Asimow P. D. and Ghiorso M. S. (1998) Algorithmic modifications extending MELTS to calculate subsolidus phase relations. *Am. Mineral*. **83**, 1127-1132.

Baker J. A., Schiller M. and Bizzarro M. (2012) ^{26}Al–^{26}Mg deficit dating ultramafic meteorites and silicate planetesimal differentiation in the early Solar System? *Geochim. Cosmochim. Acta* **77**, 415-431.

Barrat J. A., Rouxel O., Wang K., Moynier F., Yamaguchi A., Bischoff A. and Langlade J. (2015) Early stages of core segregation recorded by Fe isotopes in an asteroidal mantle. *Earth Planet. Sci. Lett*. **419**, 93-100.

Barrat J. A., Dauphas N., Gillet P., Bollinger C., Etoubleau J., Bischoff A. and Yamaguchi A. (2016a) Evidence from Tm anomalies for non-CI refractory lithophile element proportions in terrestrial planets and achondrites. *Geochim. Cosmochim. Acta* **176**, 1-17.

Barrat J. A., Jambon A., Yamaguchi A., Bischoff A., Rouget M. L. and Liorzou C. (2016b) Partial melting of a C-rich asteroid: Lithophile trace elements in ureilites. *Geochim. Cosmochim. Acta* **194**, 163-178.

Barrat J. A., Sansjofre P., Yamaguchi A., Greenwood R. C. and Gillet P. (2017) Carbon isotopic variation in ureilites: Evidence for an early, volatile-rich Inner Solar System. *Earth Planet. Sci. Lett.* **478**, 143-149.

Berkley J. L., Brown H. G., Keil K., Carter N. L., Mercier J. C. and Huss G. (1976) The Kenna ureilite: An ultramafic rock with evidence for igneous, metamorphic, and shock origin. *Geochim. Cosmochim. Acta* **40**, 1429-1437.

Bischoff A., Horstmann M., Barrat J. A., Chaussidon M., Pack A., Herwartz D., Ward D., Vollmer C. and Decker S. (2014) Trachyandesitic volcanism in the early Solar System. *Proc. Nat. Ac. Sci. USA* 111, 12689-12692.

Blundy J. D. and Wood B. J. (1991) Crystal-chemical controls on the partitioning of Sr and Ba between plagioclase feldspar, silicate melts, and hydrothermal solutions. *Geochim. Cosmochim. Acta* **55**, 193-209.

Brey G. P. and Köhler T. (1990) Geothermobarometry in four-phase lherzolites II. New thermobarometers, and practical assessment of existing thermobarometers. *J. Petrol.*

31, 1353-1378.

Budde G., Kruijer T. S., Fischer-Gödde M., Irving A. J. and Kleine T. (2015) Planetesimal differentiation revealed by the Hf–W systematics of ureilites. *Earth Planet. Sci. Lett.* **430**, 316-325.

Budde G., Burckhardt C. and Kleine T. (2017) The distinct genetics of carbonaceous and non-carbonaceous meteorites inferred from molybdenum isotopes. *80th Ann. Meet. Meteor. Soc.* 6271

Chakraborty S. (1997) Rates and mechanisms of Fe_Mg interdiffusion in olivine at 980–1300 C. *J. Geophys. Res. Solid Earth* **102**, 12317-12331.

Clayton R. N. and Mayeda T. K. (1996) Oxygen isotope studies of achondrites. *Geochim. Cosmochim. Acta* **60**, 1999-2017.

Dasgupta R., Chi H., Shimizu N., Buono A. S. & Walker D. (2013) Carbon solution and partitioning between metallic and silicate melts in a shallow magma ocean: Implications for the origin and distribution of terrestrial carbon. *Geochim. Cosmochim. Acta* **102**, 191-212.

Dobrzhinetskaya L. F. (2012) Microdiamonds—Frontier of ultrahigh-pressure metamorphism: A review. *Gondwana Res.* **21**, 207-223.

Downes H., Mittlefehldt D. W., Kita N. T. and Valley J. W. (2008) Evidence from polymict ureilite meteorites for a disrupted and re-accreted single ureilite parent asteroid gardened by several distinct impactors. *Geochim. Cosmochim. Acta* **72**, 4825-4844.

Feldstein S. N., Jones R. H. and Papike J. J. (2001) Disequilibrium partial melting experiments on the Leedey L6 chondrite: Textural controls on melting processes. *Meteorit. Planet. Sci.* **36**, 1421-1441.

Ghiorso M. S. and Sack R. O. (1995) Chemical mass transfer in magmatic processes IV. A revised and internally consistent thermodynamic model for the interpolation and extrapolation of liquid-solid equilibria in magmatic systems at elevated temperatures and pressures. *Contrib. Mineral. Petrol.* **119**, 197-212.

Goodrich C. A., Keil K., Berkley J. L., Laul J. C., Smith M. R., Wacker J. F., Clayton R.N. and Mayeda T. K. (1987) Roosevelt County 027: A low_shock ureilite with interstitial silicates and high noble gas concentrations. *Meteoritics* **22**, 191-218.

Goodrich C. A., Fioretti A. M., Tribaudino M. and Molin G. (2001) Primary trapped melt inclusions in olivine in the olivine-augite-orthopyroxene ureilite Hughes 009. *Geochim. Cosmochim. Acta* **65**, 621-652.

Goodrich C. A., Scott E. R. and Fioretti A. M. (2004) Ureilitic breccias: clues to the petrologic structure and impact disruption of the ureilite parent asteroid. *Chemie der Erde-Geochemistry* **64**, 283-327.

Goodrich C. A., Fioretti A. M. and Van Orman J. (2009) Petrogenesis of augite-bearing ureilites Hughes 009 and FRO 90054/93008 inferred from melt inclusions in olivine, augite and orthopyroxene. *Geochim. Cosmochim. Acta* **73**, 3055-3076.

Goodrich C. A., Hutcheon I. D., Kita N. T., Huss G. R., Cohen B. A. and Keil K. (2010) 53 Mn–53 Cr and 26 Al–26 Mg ages of a feldspathic lithology in polymict ureilites. *Earth Planet. Sci. Lett.* **295**, 531-540.

Goodrich C. A., Harlow G. E., Van Orman J. A., Sutton S. R., Jercinovic M. J. and Mikouchi T. (2014) Petrology of chromite in ureilites: Deconvolution of primary oxidation states and secondary reduction processes. *Geochim. Cosmochim. Acta* **135**, 126-169.

Goodrich C. A., Hartmann W. K., O'Brien D. P., Weidenschilling S. J., Wilson L., Michel P. and Jutzi, M. (2015) Origin and history of ureilitic material in the solar system: The view from asteroid 2008 TC3 and the Almahata Sitta meteorite. *Meteorit. Planet Sci*. **50**, 782-809.

Goodrich, C. A., Treiman, A. H., and Boyle, S. (2017) Melt Formation and Evolution on the Ureilite Parent Body, as Shown by Feldspathic Clasts in Polymict Ureilites. *Lun. Planet. Sci. XLVII.* #1196(abstr.).

Guan Y. and Crozaz G. (2000) Light rare earth element enrichments in ureilites: a detailed ion microprobe study. *Meteorit. Planet. Sci.* **35**, 131-144.

Guan Y. and Crozaz G. (2001) Microdistributions and petrogenetic implications of rare earth elements in polymict ureilites. *Meteorit. Planet. Sci.***36**, 1039-1056.

Guillong M., von Quadt A., Sakata S., Peytcheva I. and Bachmann O. (2014) LA-ICP-MS Pb–U dating of young zircons from the Kos–Nisyros volcanic centre, SE Aegean arc. *J. Analyt. Atom. Spectrom.* **29**, 963-970.

Ikeda Y. (1999) Petrology of the Asuka 881931 ureilite with special reference to crystallization of interstitial silicate melt. *Meteorit. Planet. Sci.* **34**, 625-636.

Ikeda Y. (2007) Petrology of an unusual monomict ureilite, NWA1241. *Polar Sci.* **1**, 45-53.

Ikeda Y. and Prinz M. (2001) Magmatic inclusions and felsic clasts in the Dar al Gani 319 polymict ureilite. *Meteorit. Planet. Sci.* **36**, 481-499.

Janots E., Gnos E., Hofmann B. A., Greenwood R. C., Franchi I. A. and Bischoff A. (2011) Jiddat al Harasis 422: A ureilite with an extremely high degree of shock melting.

Meteorit. Planet. Sci. **46**, 134-148.

Jacquet E., Alard O. and Gounelle M. (2015) Trace element geochemistry of ordinary chondrite chondrules: The type I/type II chondrule dichotomy. *Geochim. Cosmochim. Acta* **155**, 47-67.

Jercinovic M. J. and Goodrich C. A. (2011) Primary Chromite in Two More Main Group Ureilites---NWA 3109 (Fo 76) and EET 96328 (Fo 85). What Does Cr in Ureilites Tell Us? *Lun. Planet. Sci. XLII.* #1152(abstr.).

Kimura M., Sugiura N., Mikouchi T., Hirajima T., Hiyagon H. and Takehana Y. (2013) Eclogitic clasts with omphacite and pyrope-rich garnet in the NWA 801 CR2 chondrite. *Am. Mineral.* **98**, 387-393.

Kita N. T., Ikeda Y., Togashi S., Liu Y., Morishita Y. and Weisberg M. K. (2004) Origin of ureilites inferred from a SIMS oxygen isotopic and trace element study of clasts in the Dar al Gani 319 polymict ureilite. *Geochim. Cosmochim. Acta* **68**, 4213-4235.

Kovach H. A. and Jones R. H. (2010) Feldspar in type 4–6 ordinary chondrites: Metamorphic processing on the H and LL chondrite parent bodies. *Meteorit. Planet. Sci.***45**, 246264.

Lanari P., Vidal O., De Andrade V., Dubacq B., Lewin E., Grosch E. G. and Schwartz S. (2014) XMapTools: A MATLAB©-based program for electron microprobe X-ray image processing and geothermobarometry. *Comput. Geosci.* **62**, 227-240.

Lespade P., Al-Jishi R. and Dresselhaus M. S. (1982) Model for Raman scattering from incompletely graphitized carbons. *Carbon* **20**, 427-431.

Lunning N. G., Gardner-Vandy K. G., Sosa E. S., McCoy T. J., Bullock E. S. and Corrigan C. M. (2017) Partial melting of oxidized planetesimals: An experimental study to test the formation of oligoclase-rich achondrites Graves Nunataks 06128 and 06129. *Geochim. Cosmochim. Acta* **214**, 73-85.

McDonough W. F. and Sun S. S. (1995) The composition of the Earth. *Chem. Geol.* **120**, 223-253.

Miyahara M., Ohtani E., El Goresy A., Lin Y., Feng L., Zhang J. C., Gillet P., Nagase T., Muto J. and Nishijima M. (2015) Unique large diamonds in a ureilite from Almahata Sitta 2008 TC 3 asteroid. *Geochim. Cosmochim. Acta* **163**, 14-26.

Miyamoto M., Takase T. and Mitsuda Y. (1993) Raman spectra of various diamonds. *Mineral. J.* **16**, 246-257.

Mollo S., Blundy J. D., Iezzi G., Scarlato P. and Langone A. (2013) The partitioning of trace elements between clinopyroxene and trachybasaltic melt during rapid cooling and crystal growth. *Contrib. Mineral. Petrol.* **166**, 1633-1654.

Müller T., Dohmen R., Becker H. W., Ter Heege J. H. and Chakraborty S. (2013) Fe–Mg interdiffusion rates in clinopyroxene: experimental data and implications for Fe–Mg exchange geothermometers. *Contrib. Mineral. Petrol.* **166**, 1563-1576.

Newsom H. E. (1995) Composition of the solar system, planets, meteorites, and major terrestrial reservoirs. In *Global Earth Physics*: *A Handbook of Physical Constants* (Vol. 1, p. 159). *Amer. Geophys. Union.*

Qin L., Rumble D., Alexander C. M. D., Carlson R. W., Jenniskens P. and Shaddad M. H. (2010) The chromium isotopic composition of Almahata Sitta. *Meteorit. Planet. Sci.* **45**, 1771-1777.

Rubin A. E. (2006) Shock, post_shock annealing, and post_annealing shock in ureilites. *Meteorit. Planet. Sci.* **41**, 125-133.

Sanders I. S., Scott E. R. D. and Delaney J. S. (2017) Origin of mass_independent oxygen isotope variation among ureilites: Clues from chondrites and primitive achondrites. *Meteorit. Planet. Sci.* **52**, 690-708.

Sarma B., Cramb A. W. and Fruehan R. J. (1996) Reduction of FeO in smelting slags by solid carbon: experimental results. *Metall. Mater. Trans. B.* **27,** 717-730.

Schiller M., Connelly J. N., Glad A. C., Mikouchi T. and Bizzarro M. (2015) Early accretion of protoplanets inferred from a reduced inner solar system 26Al inventory. *Earth Planet. Sci. Lett*. **420**, 45-54.

Stachel T. and Luth R. W. (2015) Diamond formation—where when and how? *Lithos* **220**, 200-220.

Sumiya H., Irifune T., Kurio A., Sakamoto S. and Inoue T. (2004) Microstructure features of polycrystalline diamond synthesized directly from graphite under static high pressure. *J. Mater. Sci.* **39**, 445-450.

Toplis M. J. (2005) The thermodynamics of iron and magnesium partitioning between olivine and liquid: criteria for assessing and predicting equilibrium in natural and experimental systems. *Contrib. Mineral. Petrol.* **149**, 22-39.

TorigoyeKita N., Tatsumoto M., Meeker G. P. and Yanai K. (1995) The 4.56 Ga U□ Pb age of the MET 780058 ureilite. *Geochim. Cosmochim. Acta* **59**, 2319-2329.

Usui T., Jones J. H. and Mittlefehldt D. W. (2015) A partial melting study of an ordinary (H) chondrite composition with application to the unique achondrite Graves Nunataks 06128 and 06129. *Meteorit. Planet. Sci.* **50**, 759-781.

van Kooten E. M., Schiller M. and Bizzarro M. (2017) Magnesium and chromium isotope evidence for initial melting by radioactive decay of ^{26}Al and late stage impact-melting of the ureilite parent body. *Geochim. Cosmochim. Acta* **208**, 1-23.

Ward D., Bischoff A., Roszjar J., Berndt, J. and Whitehouse, M. J. (2017) Trace element inventory of meteoritic Ca-phosphates. *Am. Mineral.* **102**, 1856-1880.

Warren P. H. (2011) Stable-isotopic anomalies and the accretionary assemblage of the Earth and Mars: A subordinate role for carbonaceous chondrites. *Earth Planet. Sci. Lett.* **311**, 93-100.

Warren P. H. (2012) Parent body depth–pressure–temperature relationships and the style of the ureilite anatexis. *Meteorit. Planet. Sci.* **47**, 209-227.

Warren P. H. and Kallemeyn G. W. (1992) Explosive volcanism and the graphite-oxygen fugacity buffer on the parent asteroid (s) of the ureilite meteorites. *Icarus* **100**, 110126.

Warren P. H. and Huber H. (2006) Ureilite petrogenesis: A limited role for smelting during anatexis and catastrophic disruption. *Meteorit. Planet. Sci.* **41**, 835-849.

Warren P. H. and Rubin A. E. (2010) Pyroxene-selective impact smelting in ureilites. *Geochim.Cosmochim. Acta* **74**, 5109-5133.

Willems B., De Corte K. and Van Tendeloo G. (2004) Why does polycrystalline natural diamond turn black after annealing? *Phys. Status Solidi A.* **201**, 2486-2491.

Yamakawa A., Yamashita K., Makishima A. and Nakamura E. (2010) Chromium isotope systematics of achondrites: Chronology and isotopic heterogeneity of the inner solar system bodies. *Astrophys. J.* **720,** 150

Zurfluh F. J., Hofmann B. A., Gnos E., Eggenberger U. and Jull, A. T. (2016) Weathering of ordinary chondrites from Oman: Correlation of weathering parameters with ^{14}C terrestrial ages and a refined weathering scale. *Meteorit. Planet. Sci.* **51**, 1685-1700.

Table 1. Representative EMPA (oxides in wt%) of primary phases in RaS 517 (Mg# = Mg/(Mg+Fe); Cr# = Cr/(Cr+Al)).

	Aug						Low-Ca			
	core	core	core	avg. core (n=23)	Std. dev.	low FeO	core	core	avg. core (n=10)	Std. dev.
SiO_2	52.40	52.44	52.51	52.48	0.40	53.20	54.29	53.86	54.17	0.21
Al_2O_3	2.83	2.85	2.84	2.84	0.03	2.80	1.70	1.69	1.70	0.02
CaO	15.75	15.81	15.87	15.71	0.44	17.24	2.01	2.10	2.06	0.05
Na_2O	1.17	1.15	1.16	1.15	0.07	0.86	0.19	0.23	0.21	0.01
FeO	6.99	7.17	7.19	7.10	0.29	5.88	12.37	12.19	12.26	0.15
MnO	0.37	0.36	0.36	0.36	0.01	0.36	0.43	0.43	0.43	0.00
TiO_2	0.24	0.24	0.22	0.23	0.01	0.21	0.10	0.10	0.10	0.00
MgO	17.57	17.56	17.60	17.60	0.18	17.98	28.19	28.30	28.06	0.24
Cr_2O_3	2.04	2.01	2.02	2.02	0.03	1.95	1.06	1.09	1.09	0.02
Total	99.35	99.58	99.76	99.49	0.59	100.48	100.34	99.98	100.08	0.34
Mg#	81.8	81.4	81.4	81.4	0.2	84.5	80.4	80.5	80.3	0.2
Wo	34.5	34.5	34.5	34.3	0.5	36.8	4.0	4.1	4.1	0.1

	Ol						Spn			
	core	core	core	avg. core (n=38)	Std. dev.	low FeO		high FeO	low FeO	low FeO
SiO_2	38.36	38.43	38.37	38.26	0.19	40.82	SiO_2	0.08	0.08	0.07
Al_2O_3	0.05	0.03	0.03	0.04	0.02	0.02	Al_2O_3	18.39	18.11	19.31
CaO	0.22	0.22	0.21	0.22	0.01	0.25	CaO	0.00	0.00	0.01
FeO	21.04	21.28	21.20	21.08	0.32	4.53	FeO	20.64	2.58	7.35
MnO	0.47	0.46	0.46	0.46	0.01	0.57	MnO	1.00	0.59	1.37
TiO_2	0.01	0.01	0.01	0.01	0.00	0.04	TiO_2	0.69	0.78	0.78
MgO	39.55	40.46	40.22	40.48	0.35	52.83	MgO	9.79	20.93	17.81
Cr_2O_3	0.37	0.36	0.36	0.37	0.04	1.82	Cr_2O_3	49.69	58.64	53.57
Total	100.05	101.24	100.85	100.90	0.40	100.88	Total	100.29	101.71	100.27

Fo	77.0	77.2	77.2	77.4	0.4	95.4	Mg#	45.8	93.5	81.2
Fe/Mn	44.6	46.0	45.9	45.7	1.2	7.9	Cr#	64.5	68.5	65.0

Abbreviations: Throughout. Aug, augite, Low-Ca, low-Ca pyroxene, Ol, olivine, Spn, spinel.

Table 2. EMPA (oxides in wt%) of RaS 517 glass and secondary pyroxene in glass (Mg# = Mg/(Mg+Fe)). Last separate SEM-EDX analyses (oxides in wt%) of glass.

EMPA Glass

SiO_2	72.36	72.80	73.53	74.82	75.14	75.54	76.05	76.47	76.55	76.94	77.26	77.51	78.79	79.71	79.85	83.67	72.40
Na_2O	2.87	2.25	1.95	0.97	1.63	2.11	2.18	2.21	2.67	2.56	0.98	2.52	1.11	1.44	1.96	1.97	5.59
CaO	1.09	0.52	0.56	0.80	0.27	0.36	0.27	0.37	0.33	0.29	0.34	0.25	0.19	0.19	0.12	0.16	1.03
K_2O	0.90	1.05	1.04	0.89	1.04	1.01	1.04	0.98	1.02	0.99	0.78	1.01	0.95	1.04	0.99	0.53	0.92
Al_2O_3	18.60	15.58	15.38	16.31	13.65	14.78	14.27	14.72	13.98	14.01	14.51	13.76	13.04	10.69	12.13	9.10	18.69
MnO	0.05	0.04	0.04	0.05	0.02	0.01	0.03	0.01	0.02	0.01	0.03	0.01	0.04	0.01	0.00	0.01	0.00
FeO	0.58	0.65	0.88	0.85	1.31	1.01	1.01	0.92	0.88	0.89	1.48	0.90	1.02	0.91	1.24	1.49	0.20
MgO	0.39	0.74	0.69	0.46	1.23	0.90	0.55	0.29	0.62	0.54	0.38	0.51	0.17	0.50	0.16	0.21	0.10
TiO_2	0.26	0.27	0.30	0.30	0.27	0.29	0.29	0.23	0.26	0.25	0.28	0.26	0.24	0.15	0.20	0.13	0.55
Cr_2O_3	0.04	0.01	0.04	0.02	0.03	0.02	0.00	0.02	0.06	0.02	0.02	0.02	0.01	0.01	0.01	0.00	0.53
Total	97.14	93.90	94.42	95.47	94.59	96.02	95.69	96.22	96.40	96.50	96.06	96.76	95.55	94.64	96.66	97.27	100.01
EMPA														En			
	High-Ca																
SiO_2	56.01	53.37	55.30	53.38	55.31	55.28	53.58	55.26	54.21	54.42	55.00	53.30	53.88	58.24	58.66	58.18	58.31
Al_2O_3	0.69	1.33	1.17	2.52	0.70	0.84	1.27	0.89	1.10	1.02	1.07	2.05	2.20	1.20	0.64	1.96	0.78
MnO	0.47	0.47	0.50	0.00	0.45	0.43	0.42	0.46	0.45	0.43	0.38	0.36	0.37	0.62	0.00	0.50	0.39
FeO	2.90	1.86	1.51	4.37	1.52	1.12	3.71	2.38	3.73	3.49	2.26	0.92	0.95	2.73	0.92	1.20	0.83
MgO	23.05	21.90	22.23	18.24	22.38	23.07	18.93	21.15	19.64	19.77	20.39	20.00	20.45	34.56	36.78	34.07	36.44
TiO_2	0.22	0.30	0.39	0.28	0.29	0.32	0.22	0.22	0.31	0.31	0.26	0.26	0.27	0.07	0.16	0.23	0.18
Cr_2O_3	0.57	0.88	0.58	1.80	0.56	0.56	2.06	0.62	1.11	1.05	0.57	0.73	0.78	0.92	0.38	0.99	0.62
Na_2O	0.26	0.33	0.39	1.33	0.28	0.25	0.55	0.31	0.50	0.43	0.23	0.27	0.31	0.13	0.02	0.11	0.10
CaO	16.72	17.97	18.22	18.28	18.42	18.71	18.86	18.96	18.97	19.28	20.38	20.80	21.11	1.86	2.26	2.57	2.62
Total	100.90	98.41	100.30	100.19	99.90	100.56	99.60	100.25	100.03	100.21	100.54	98.69	100.32	100.33	99.86	99.82	100.26
Mg#	93.41	95.45	96.33	88.15	96.33	97.36	90.10	94.06	90.37	90.99	94.15	97.50	97.46	95.76	98.61	98.06	98.74
Wo	32.75	36.01	36.20	38.83	36.30	36.20	39.21	37.73	38.55	38.94	40.34	42.15	41.96	3.57	4.17	5.05	4.85
EDX	Glass																
Na_2O	6.5	7.8	8.0	8.8	8.9	8.9	9.0	9.0	9.2	9.4	9.4	9.5	9.6	10.6	11.3	12.9	13.9
Al_2O_3	11.7	13.9	13.6	17.0	14.7	17.6	18.1	17.0	17.6	19.1	19.6	18.7	20.0	18.9	18.0	20.1	21.7
SiO_2	78.5	75.8	74.2	70.1	74.7	70.2	69.6	71.2	69.6	67.5	67.3	68.7	66.6	67.0	67.9	63.8	61.4
K_2O	0.6	1.1	0.9	0.8	1.0	0.8	0.9	0.8	0.9	1.0	0.8	0.9	0.8	0.9	1.0	1.0	0.9
CaO 0.7	0.6	1.0	1.5	0.4	1.2	1.1	0.5	1.5	1.7	1.6	0.6	1.7	FeO 0.6	n.d.	n.d.	0.5	0.4	n.d.	n.d.	n.d.	n.d.	n.d.	n.d.	n.d.	1.3	0.7	1.2	1.0
MgO	1.4	0.8	2.3	1.2	n.d.	1.2	1.3	1.4	1.2	1.4	1.4	1.6	1.4	n.d.	n.d.	n.d.	n.d.
														1.4	1.1	1.1	1.2

Abbreviations: Throughout. High-Ca, high-Ca pyroxene, En, enstatite, n.d., not determined

Table 3. Trace element concentrations and oxide concentrations measured in primary silicates and glass using LA-ICP-MS

		Ol				Low-Ca Aug							
SiO_2*	wt%	38	38	38	38	54	54	54	54	53	53	53	53
TiO_2	wt%	0.01	0.01	0.01	0.01	0.09	0.09	0.10	0.11	0.21	0.23	0.23	0.23
Al_2O_3	wt%	0.03	0.04	0.03	0.03	1.68	1.67	1.82	1.86	2.82	3.04	3.03	3.04
FeO	wt%	19.52	20.41	21.05	20.60	11.60	11.49	11.94	12.26	7.26	7.10	7.07	7.11
CaO	wt%	0.20	0.22	0.23	0.22	2.00	2.01	2.20	2.26	15.50	16.73	16.74	16.82
Sc	µg/g	4.48	4.95	4.73	4.92	16.66	16.87	18.52	19.07	48.03	53.78	53.54	53.79
V	µg/g	40.02	42.15	43.18	41.72	151.83	151.15	161.23	163.71	384.51	406.90	407.19	406.89
Rb	ng/g	b.d.	b.d.	b.d.	b.d.	b.d.	b.d.	b.d.	b.d.	92	32	b.d.	33
Sr	ng/g	64	b.d.	46	b.d.	241	236	265	348	11933	12622	12829	12664
Y	ng/g	77	93	87	85	913	804	949	960	5592	6207	6087	6143
Zr	ng/g	b.d.	30	31	26	533	561	602	632	4669	5396	5311	5277
Cs	ng/g	b.d.	b.d.	b.d.	b.d.	b.d.	b.d.	b.d.	b.d.	b.d.	b.d.	b.d.	b.d.
Ba	ng/g	b.d.	b.d.	b.d.	46	b.d.	b.d.	b.d.	b.d.	b.d.	b.d.	b.d.	b.d.
La	ng/g	b.d.	b.d.	b.d.	b.d.	7	b.d.	5	7	269	291	282	283
Ce	ng/g	b.d.	b.d.	2	b.d.	21	22	20	28	929	998	989	975
Pr	ng/g	b.d.	b.d.	b.d.	b.d.	6	4	5	4	160	183	179	178
Nd	ng/g	b.d.	b.d.	b.d.	b.d.	26	b.d.	32	38	1010	1097	1029	1119
Sm	ng/g	b.d.	b.d.	b.d.	b.d.	b.d.	19	27	18	446	477	461	487
Eu	ng/g	b.d.	b.d.	b.d.	b.d.	b.d.	b.d.	7	12	135	126	118	131
Gd	ng/g	b.d.	b.d.	b.d.	b.d.	b.d.	b.d.	61	44	656	781	748	731
Tb	ng/g	b.d.	b.d.	b.d.	1	13	17	15	14	125	142	143	148
Dy	ng/g	b.d.	10	10	13	114	125	121	146	990	1056	1053	1080
Ho	ng/g	2	3	2	3	29	34	37	32	227	244	243	240
Er	ng/g	14	17	13	13	126	129	140	119	656	743	739	729
Tm	ng/g	b.d.	3	4	4	22	18	24	20	93	100	101	105
Yb	ng/g	37	36	28	27	186	171	183	179	628	687	737	666

Lu	ng/g	5 Glass	9	8	8	30	29	31	28	101	102	103	96
SiO_2	wt%	69.15	67.80	70.51	72.87	71.02	67.33	70.37	71.90	67.52	69.93	77.13	69.31
TiO_2	wt%	0.25	0.26	0.29	0.28	0.27	0.22	0.19	0.20	0.19	0.20	0.23	0.18
Al_2O_3*	wt%	14	15	15	15	15	15	14	16	17	14	14	14
FeO	wt%	3.95	1.12	0.16	0.47	0.17	0.14	0.16	0.08	0.22	0.43	0.52	0.08
CaO	wt%	0.56	0.70	0.58	0.66	0.48	0.34	0.64	0.85	1.60	4.26	4.28	0.75
Sc	µg/g	11.99	8.49	10.98	7.72	11.80	11.31	3.91	4.07	b.d.	7.99	9.46	b.d.
V	µg/g	34.76	17.11	4.33	14.56	3.44	2.63	2.48	1.37	3.20	15.76	25.80	3.71
Rb	µg/g	30.48	31.63	35.87	33.59	35.23	37.24	35.36	35.46	30.95	27.87	30.66	36.49
Sr	µg/g	72.44	83.31	92.71	93.32	82.98	53.31	80.18	116.80	143.09	107.47	92.22	61.43
Y	µg/g	5.23	4.94	6.52	5.67	4.90	5.14	3.10	3.33	3.63	3.64	3.88	2.22
Zr	µg/g	29.26	30.05	33.49	32.40	29.68	26.95	29.28	34.05	37.35	27.93	28.83	29.39
Cs	µg/g	1.90	2.12	2.18	2.05	2.16	2.22	2.23	2.05	1.84	1.65	1.90	2.65
Ba	µg/g	49.93	61.83	70.64	72.44	65.21	43.82	56.99	81.46	96.20	73.09	65.69	49.10
La	µg/g	2.85	3.31	3.23	3.41	2.56	2.05	2.48	3.61	3.99	3.19	2.71	2.20
Ce	µg/g	5.64	5.83	6.29	6.30	5.06	4.33	4.10	6.14	6.73	5.55	4.53	3.37
Pr	µg/g	0.62	0.63	0.68	0.69	0.60	0.36	0.37	0.57	0.67	0.53	0.49	0.32
Nd	µg/g	2.00	2.54	2.84	2.57	2.24	1.68	1.82	2.35	2.16	2.21	2.09	1.57
Sm	µg/g	0.64	0.91	0.53	0.75	0.45	0.34	0.73	0.63	0.81	0.79	0.37	b.d.
Eu	µg/g	0.48	0.34	0.47	0.50	0.42	0.16	0.43	0.50	0.70	0.52	0.38	0.23
Gd	µg/g	b.d.	b.d.	b.d.	1.12	0.80	b.d.	b.d.	0.70	b.d.	0.76	b.d.	b.d.
Tb	µg/g	0.12	0.14	0.16	0.17	0.14	0.12	0.08	0.07	0.07	0.10	0.06	0.09
Dy	µg/g	0.88	0.88	1.14	1.23	0.71	1.12	0.51	0.56	0.50	0.75	0.53	0.27
Ho	µg/g	0.16	0.18	0.24	0.18	0.20	0.23	0.12	0.14	0.16	0.09	0.11	0.08
Er	µg/g	0.51	0.57	0.78	0.83	0.53	0.50	0.32	0.38	0.26	0.47	0.44	0.20
Tm	µg/g	0.10	0.09	0.11	0.13	0.10	0.06	0.09	0.04	0.05	0.07	0.06	0.07
Yb	µg/g	0.59	0.90	0.64	0.58	0.38	b.d.	0.47	0.59	0.65	0.75	0.56	0.29
Lu	µg/g	0.12	0.10	0.12	0.11	0.06	0.08	0.06	0.06	0.07	0.06	0.09	0.07

*EMPA for internal standardization *Abbreviations:* Throughout. Aug, augite, Low-Ca, low-Ca pyroxene, Ol, olivine, b.d., below detection limit

Table 4. Ureilites with Al-Si-rich glass

Sample	Fo	Pyroxene type	Reference
LEW 88774	74	Low-Ca, Aug	*Goodrich et al. 2014*
LAP 03587	75	Pigeonite	*Warren and Rubin 2010*
RaS 517	77	Low-Ca, Aug	*This study*
HaH 064	78	Low-Ca, Aug	*Goodrich et al. 2014*
JaH 422	78	Low-Ca, Aug	*Janots et al. 2011*
Asuka 881931	79	Pigeonite	*Ikeda 1999*
Kenna	79	Pigeonite	*Berkley et al. 1976*
NWA 1241	80*	Pigeonite	*Ikeda 2007*
RC 027	80	Pigeonite	*Goodrich et al. 1987*
NWA 2624	80	"Low-Ca pigeonite"	*Meteoritical Bulletin*
LAR 04315	82	Pigeonite	*Warren and Rubin 2010*
EET 96328	85	Orthopyroxene	*Jercinovic and Goodrich 2011*
Hughes 009	87	Low Ca, Aug	*Goodrich et al. 2001*
FRO 90054	87	Low-Ca, Aug	*Goodrich et al. 2009*

*Lowest range from *Meteoritical Bulletin Database* Table 5. Results from geothermometry (Brey and Köhler 1990; MELTS Ol-Spn-Opx) and oxybarometry (MELTS Ol-Spn-Opx) for primary unreduced mineral compositions followed by parameters used to calculate bulk compositions and results from MELTS calculations: Last, olivine-melt Fe-Mg partitioning from MELTS results and corresponding modelled values for alkali and silica dependent partitioning (Toplis et al., 2005) of results from MELTS and MELTS liquids normalized to 3 mol% lower SiO_2 contents.

Pyroxene-pair geothermometer and Ol-Spn-Opx geothermometer-oxybarometer

Pressure	Bar	100	1000	10000
Brey and Köhler	T (°C)	1142	1144	1170
Ol-Spn-Opx	T (°C)	1152	1161	1252
Ol-Spn-Opx	logfO_2	-13.8	-13.7	-12.3

Bulk composition calculation parameters

	Ol	Low-Ca	Aug	Glass	Bulk

Density	(g/cm^3)	3.5	3.3	3.2	2.6	3.4		
Phase proportion	wt%	60.7	30.9	8.4	0.5	100		
MELTS results								
Pressure	Bar	100	100	100	100	100	100	100
Temperature	T (°C)	1140	1145	1150	1155	1160	1165	1170
Oxygen fugacity	logfO_2	-14.0	-13.9	-13.9	-13.8	-13.8	-13.7	-13.6
Olivine	wt%	64	64	64	64	64	64	64
Orthopyroxene	wt%	27	27	27	27	27	27	16
Clinopyroxene	wt%	5	5	5	4	4	4	15
Melt	wt%	3	3	3	3	3	4	4
Spinel	wt%	1	1	1	1	1	1	1
Fo		78	78	78	78	78	78	78
Opx Mg#		80	80	80	80	80	80	80
Cpx Mg#		82	82	81	81	81	81	78
Cpx Wo		36	35	35	35	34	33	14
	Liquid							
SiO_2	wt%	63.3	62.7	62.4	62.0	61.7	61.3	61.5
Al_2O_3	wt%	11.9	12.1	12.0	11.8	11.7	11.5	11.1
FeO_{tot}	wt%	6.1	6.3	6.6	6.8	7.1	7.4	7.5
MgO	wt%	3.8	4.0	4.2	4.4	4.6	4.8	5.0
CaO	wt%	6.2	6.5	6.8	7.1	7.4	7.7	7.7
$Na_2O + K_2O$	wt%	8.2	7.8	7.5	7.2	6.8	6.5	6.5
	Mg#	54	55	55	55	55	55	56
Ol-Melt Fe-Mg exchange								
From MELTS olivine and liq.	$K_{Dol\text{-}liq}$	0.34	0.34	0.34	0.34	0.34	0.35	0.35
From MELTS liq. using Toplis (2005)	$K_{Dol\text{-}liq}$	0.33	0.33	0.33	0.33	0.34	0.34	0.34
From MELTS liq. -3 mol% SiO_2 using Toplis (2005)	$K_{Dol\text{-}liq}$	0.33	0.34	0.34	0.34	0.34	0.34	0.34

Fig. 1. RaS 517 main mineral assemblage. (a) Olivine with Fe-depleted, reduced rims (darker), matrix augite and augite enclosed in low-Ca pyroxene, showing smooth grain contacts. White are Fe metal and Fe-hydroxides, carbon phases are black (BSE). (b) Large low-Ca pyroxene (red outline) grain enclosing augite, partly reduced olivine (example grain in inset with enhanced contrast, yellow outline) and black graphite (gr) laths (BSE). (c)

Skeletal Cr-spinel with scalloped rim towards intergrown carbon (dark) and metal (white). Grain segment with higher reflectivity is marked with yellow outline (refl. light) and shown in contrast enhanced inset of the corresponding image segment.

Fig. 2. Glass (gl) veinlets and related textures in RaS 517 (BSE). (a) High-Ca pyroxene with euhedral termination in glass, intergrown with reduced olivine rims. High-Ca pyroxene of similar composition has grown on primary low-Ca pyroxene altered rims. Less abundant enstatite-dominated dendrites are concentrated on primary silicate rims adjacent to carbon and metal. (b) Glass veinlet with metal/sulfide globules where secondary high-Ca pyroxene has crystallized on primary low-Ca pyroxene. (c) Dense enstatite-dominated dendrites on primary augite adjacent to metal and carbon. (d) Glass adjacent to spinel (shown in Fig. 1c) hosting secondary spinel with metal inclusions. Very fine-grained material in outer glass rim mainly consists of spinel and pyroxene. (e) Glass veinlet in low-Ca pyroxene hosting (Fe,Ni)phosphide (abbr. "p") with euhedral termination in glass.

Fig. 3. Element maps (EMPA) showing element distribution in glass veinlets and associated phases. (a) The dark red bands (highest counts for Mg) on primary silicate rims (aug, low-Ca) correspond to enstatite dendrites. These are surrounded by irregular patches with elevated Si. Mg counts are elevated where primary augite has reacted in direct contact with melt. Al and K maps outline the distribution of glass along grain boundaries. Color depicting Al in glass was normalized to average counts within set range using XMapTools (Lanari et al., 2014). (b) BSE image of glass veinlet with annotated phases included for visual reference. Al in glass is gradually increasing while Si is decreasing with increasing distance from carbon-metal assemblage. High-Ca pyroxene has crystallized on olivine and low-Ca pyroxene rims where glass shows low Si-enrichment.

Fig. 4. Ternary diagrams with oxide components (CaO, FeO, MgO, TiO_2, Na_2O and K_2O) against SiO_2 and Al_2O_3 measured in glass (wt%). Grey vectors indicate the modification of glass compositions with low SiO_2 caused by crystallization of secondary high-Ca pyroxene and addition of silica. Alkali oxide diagrams depict data from EDX measurements, all other depict data from EMPA.

Fig. 5. Liquid compositions obtained with MELTS compared to measured compositions in RaS 517 and published data. Color coded rectangles correspond to MELTS liquid composition ±1 wt% major oxides at 1140-1170°C. Black cross corresponds to EDX measurement of glass with

lowest SiO_2 (Table. 2). (a) TAS diagram (after Le Bas et al., 1986) with Almahata Sitta clast, ALM-A (blue button) data from Bischoff et al. (2014) and experimental glass obtained by Usui et al. (2015) at 1130 °C (blue cross; bars correspond to the stated standard deviation). Grey field outlines the modification of glass composition caused by crystallization of measured secondary high-Ca pyroxene. (b) Ternary diagram (normalized oxide wt% in SiO_2-Al_2O_3-CaO system). Dashed line connects glass (low SiO_2) with average high-Ca pyroxene (EMPA range in grey field) hosted in glass. ALM-A, experimental glass and glass in LEW 88774 (blue square) correspond to a mixture of these components. Calculated MELTS liquids are more silicic. Bulk ordinary chondrite (Newsom, 1995) and RaS 517 silicate compositions shown for comparison. LEW 88774 glass composition is from Warren and Rubin (2010).

Fig. 6. Diagrams depicting CI-normalized (McDonough and Sun, 1995) trace element concentrations. (a) Measured REE and Sr in glass and reconstructed values in melt from partitioning with primary augite and low-Ca pyroxene in RaS 517 using same value of D(crystal/melt) for Eu and Sr. (b) Bulk silicate REE-concentrations in RaS 517 compared with bulk ureilite measurements (Group A and B) from Barrat et al. (2016b). Representative modal contributions to the calculated bulk are shown for augite (high) low-Ca pyroxene (medium) and olivine (low). Augite and calculated bulk correspond to least depleted group A pattern. Low-Ca pyroxene corresponds to Group B pattern. (c) Lithophile trace elements ordered by compatibility. Almahata Sitta trachyandesite clast trace elements (data from Bischoff et al., 2014) show slight depletion of LREE and minor positive anomalies of Ba, Zr, Sr and Eu. Average RaS 517 glass (black line high) is enriched in LREE and shows marked positive anomalies of Ba, Zr, Sr and Eu. Trace elements in combined RaS 517 silicates (black line low) show depletion of LREE and negative anomalies of Zr, Sr, Eu and Ti. Rb was below detection in olivine and Low-Ca pyroxene, Ba below detection in augite and low-Ca pyroxene, (d) Ba plotted against Ba/Sr for feldspar in Saint Séverin LL6 (data from Kovach et al., 2010), feldspar in DaG 319 clasts (data from Kita et al., 2004) and glass in RaS 517. DaG 319 feldspar is grouped by depletion of Ba relative to Sr and marked with corresponding ranges of An. Vectors indicate the influence of silica addition and crystallization of secondary pyroxene on the glass composition in RaS 517. Crosses represent the calculated average concentrations of Ba and Sr in the earliest and latest formed melt fractions (F) during fractional melting of an ordinary chondrite mineral assemblage containing albitic feldspar. Bulk Ba and Sr starting concentration used correspond to LL chondrites (Newsom, 1995). Partitioning coefficients used, (D_{Ba}=2.00

and D_{Sr}=8.35) for plagioclase (An 5) at 1170 °C were calculated using the model of Blundy and Wood (1991).

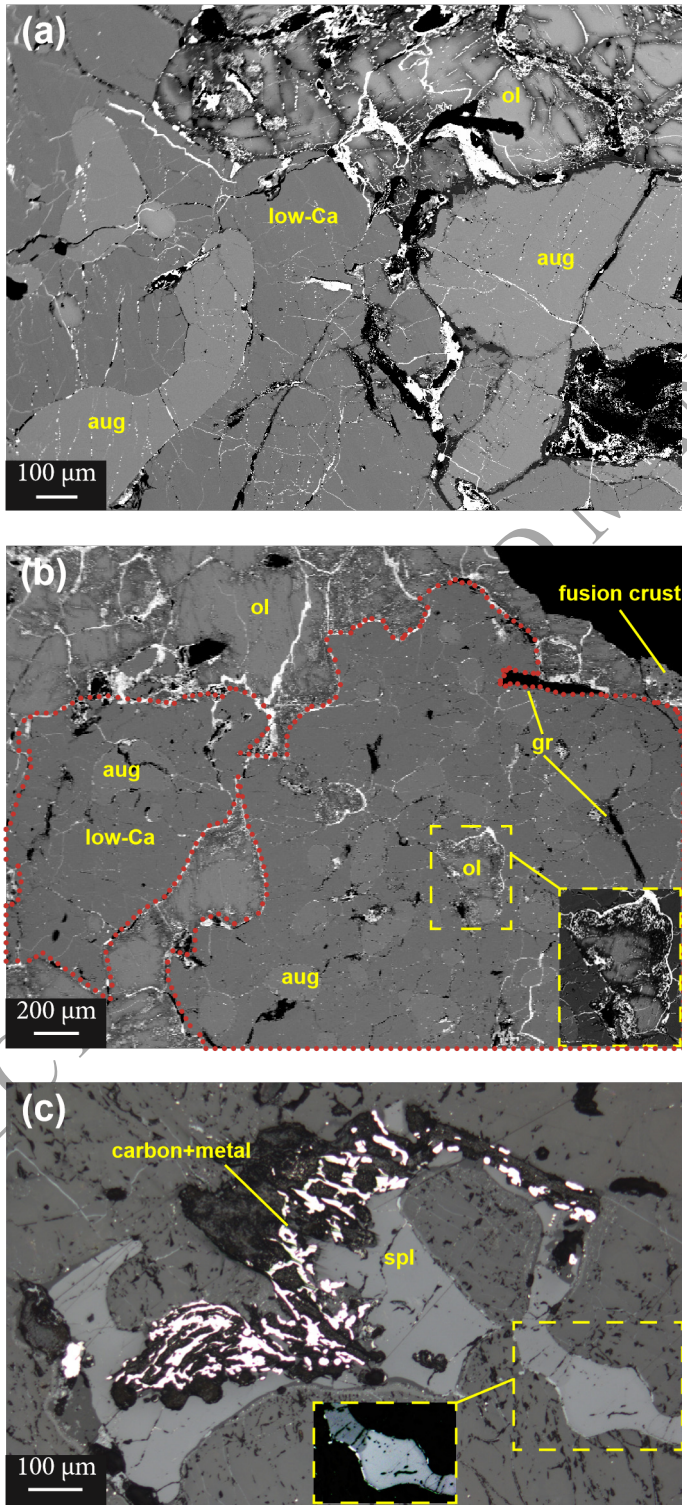

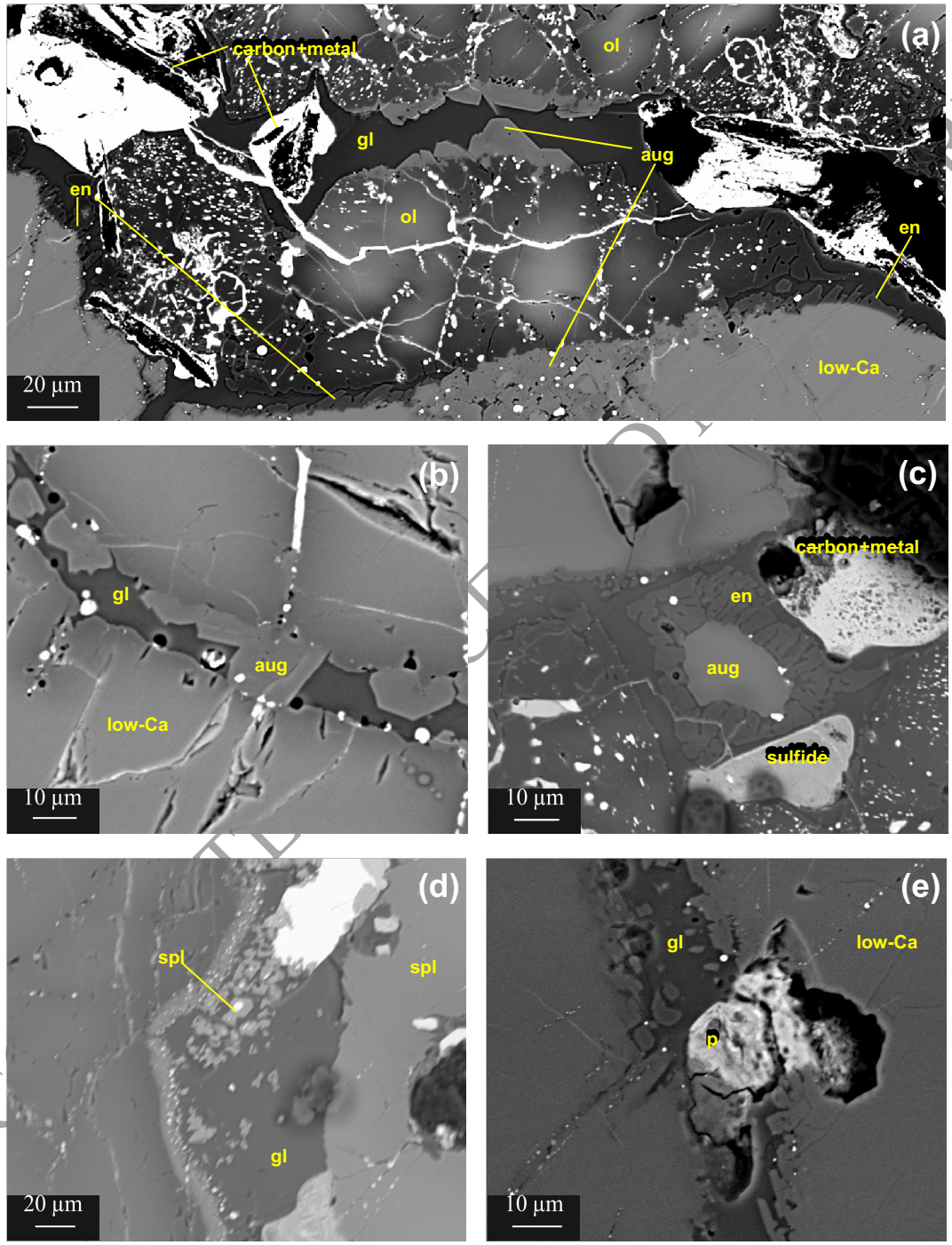

Figure3

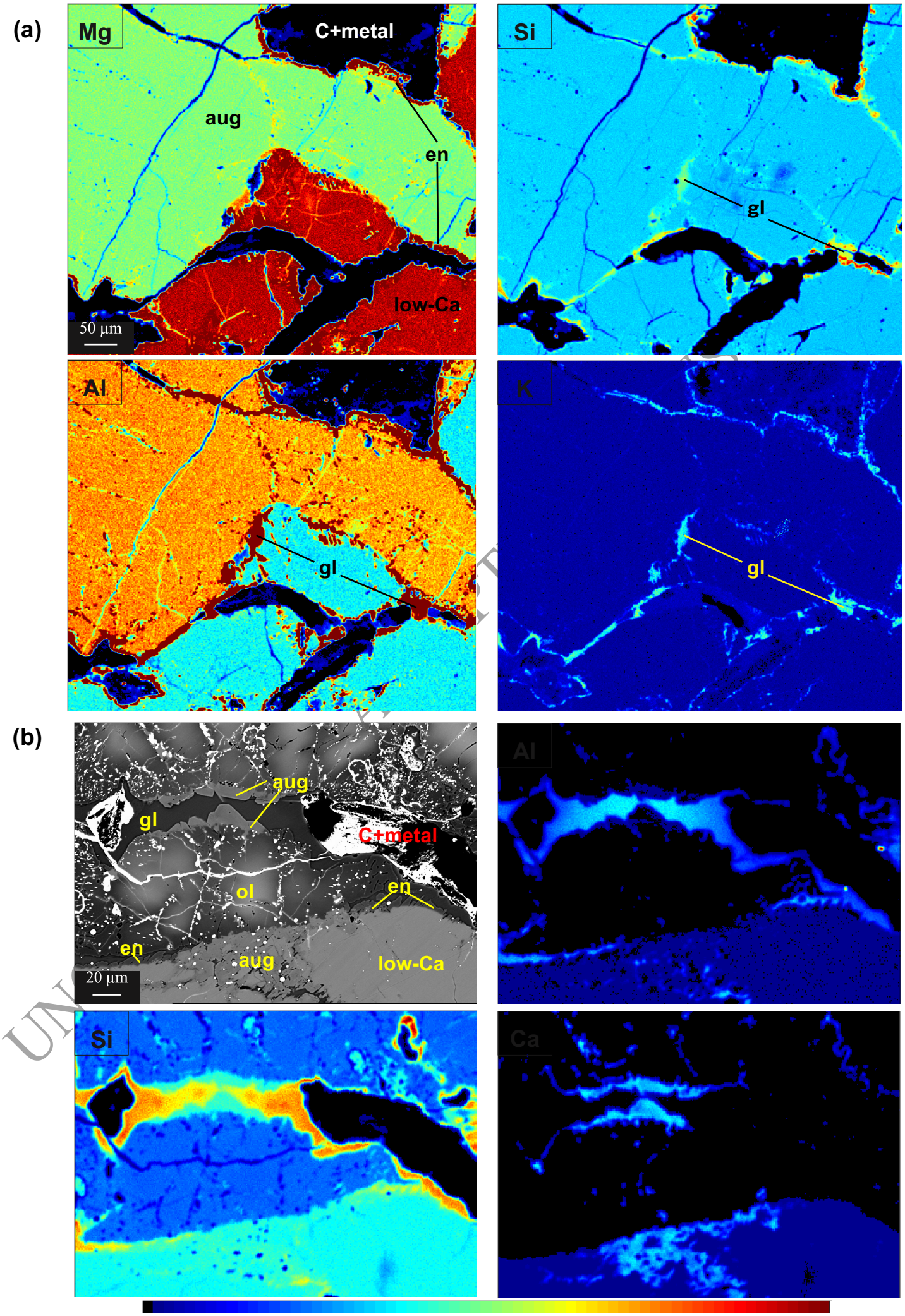
(a)
Mg
C+metal
aug
en
low-Ca
50 μm
Si
gl
Al
gl
K
gl
(b)
aug
gl
C+metal
ol
en
en
aug
low-Ca
20 μm
Al
Si
Ca
Relative element counts

Figure4

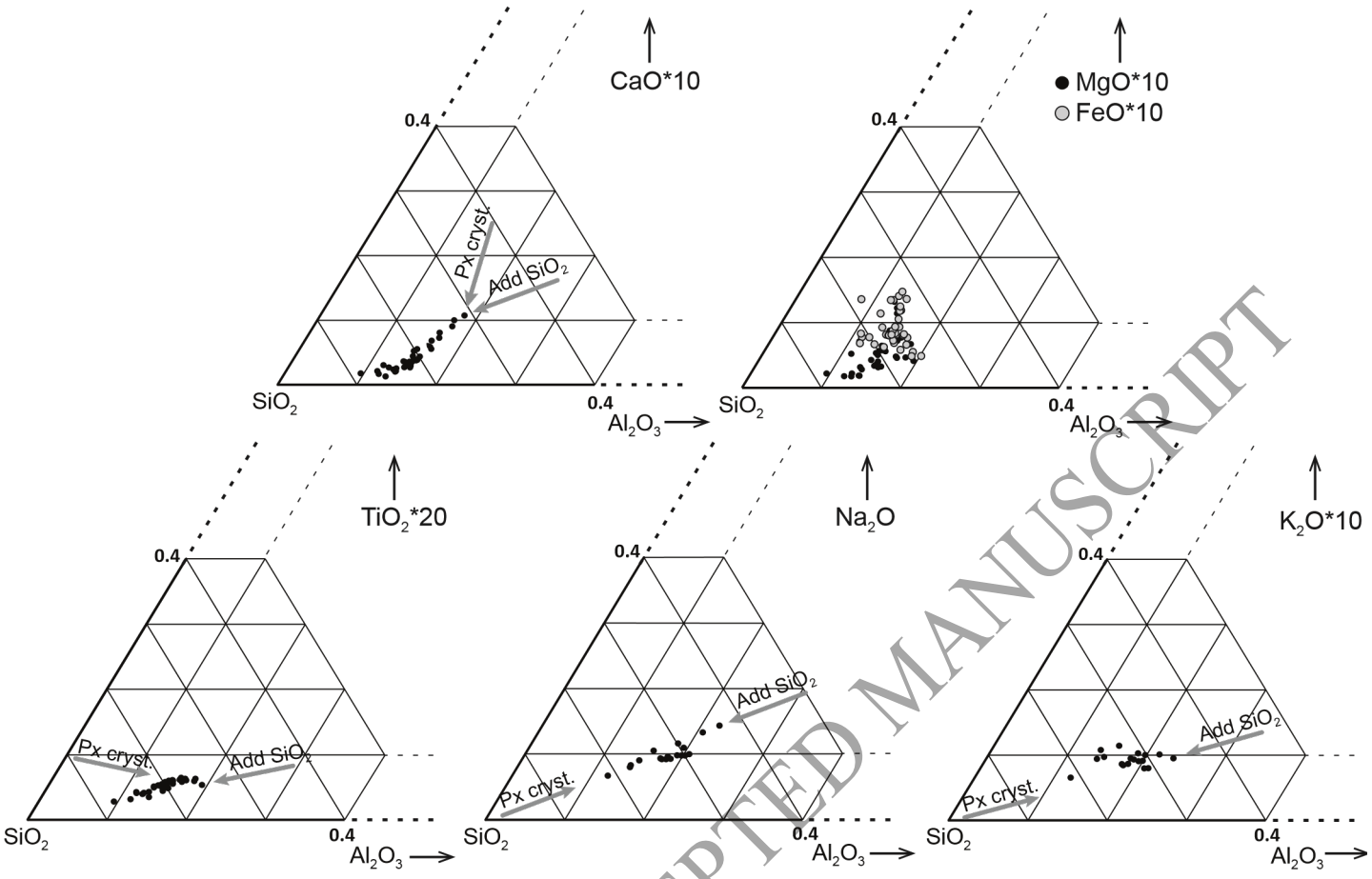

Figure5

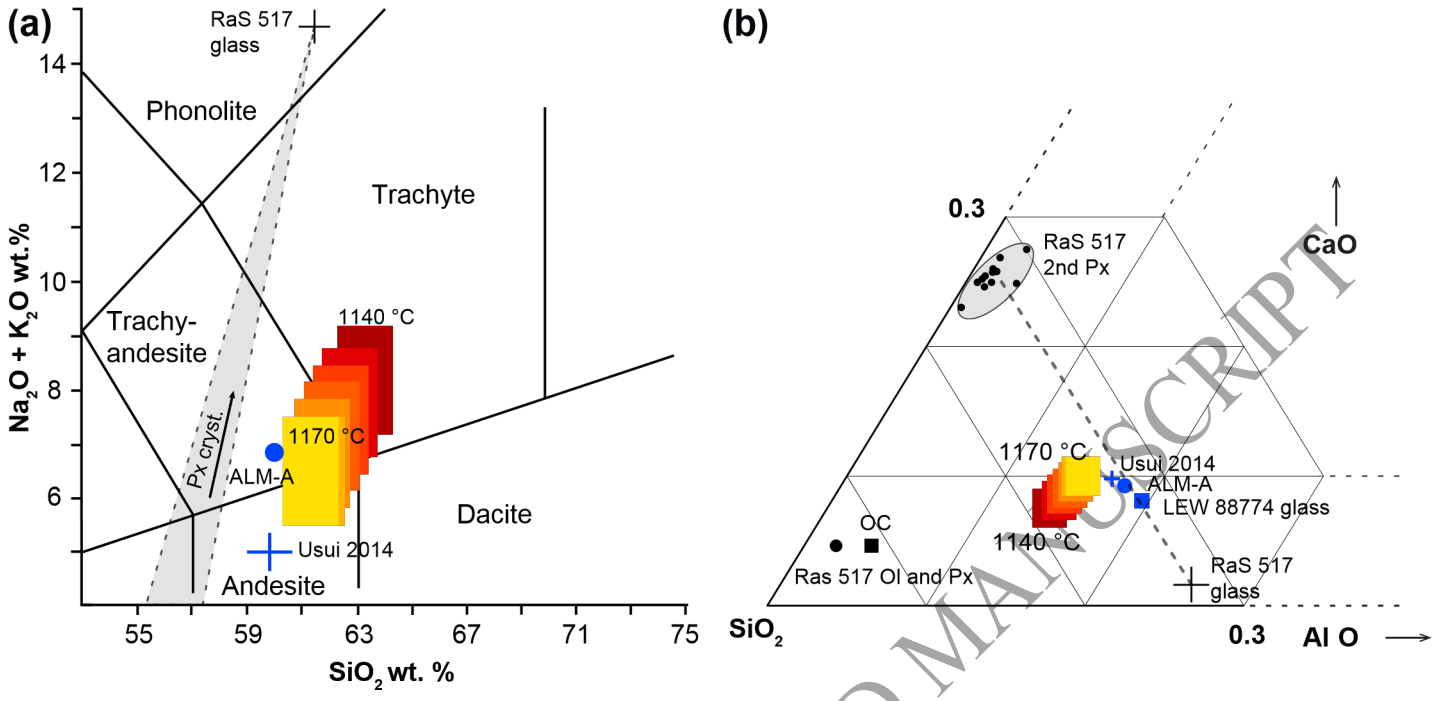

Figure6